

Hubble Asteroid Hunter

II. Identifying strong gravitational lenses in HST images with crowdsourcing

Emily O. Garvin^{1*}, Sandor Kruk^{2,3**}, Claude Cornen⁴, Rachana Bhatawdekar³, Raoul Cañameras⁵, Bruno Merín⁶

¹ Institute for Particle Physics and Astrophysics, ETH Zürich, Wolfgang-Pauli-Strasse 27, 8093 Zürich, Switzerland

² Max-Planck-Institut für Extraterrestrische Physik (MPE), Giessenbachstrasse 1, D-85748 Garching bei München, Germany

³ European Space Agency (ESA), European Space Research and Technology Centre (ESTEC), Keplerlaan 1, 2201 AZ Noordwijk, The Netherlands

⁴ Citizen Scientist, Zooniverse, Astrophysics Sub-department, University of Oxford, Keble Road, Oxford, OX1 3NP, UK

⁵ Max-Planck-Institut für Astrophysik (MPA), Karl-Schwarzschild-Straße 1, D-85748 Garching bei München, Germany

⁶ European Space Agency (ESA), European Space Astronomy Centre (ESAC), Camino Bajo del Castillo s/n, 28692 Villanueva de la Cañada, Madrid, Spain

Received April 9, 2022; revised June 10, 2022; accepted June 28, 2022

ABSTRACT

Context. The *Hubble Space Telescope* (HST) archives constitute a rich dataset of high resolution images to mine for strong gravitational lenses. While many HST programs specifically target strong lenses, they can also be present by coincidence in other HST observations.

Aims. We aim to identify non-targeted strong gravitational lenses in almost two decades of images from the ESA *Hubble Space Telescope* archive (eHST), without any prior selection on the lens properties.

Methods. We used crowdsourcing on the Hubble Asteroid Hunter (HAH) citizen science project to identify strong lenses, alongside asteroid trails, in publicly available large field-of-view HST images. We visually inspected 2 354 objects tagged by citizen scientists as strong lenses to clean the sample and identify the genuine lenses.

Results. We report the detection of 252 strong gravitational lens candidates, which were not the primary targets of the HST observations. 198 of them are new, not previously reported by other studies, consisting of 45 A grades, 74 B grades and 79 C grades. The majority are galaxy-galaxy configurations. The newly detected lenses are, on average, 1.3 magnitudes fainter than previous HST searches. This sample of strong lenses with high resolution HST imaging is ideal to follow-up with spectroscopy, for lens modelling and scientific analyses.

Conclusions. This paper presents an unbiased search of lenses, which enabled us to find a high variety of lens configurations, including exotic lenses. We demonstrate the power of crowdsourcing in visually identifying strong lenses and the benefits of exploring large archival datasets. This study shows the potential of using crowdsourcing in combination with artificial intelligence for the detection and validation of strong lenses in future large-scale surveys such as ESA's future mission *Euclid* or in JWST archival images.

Key words. Gravitational lensing: strong – Galaxies: general – Galaxies: individual

1. Introduction

Strong gravitational lensing is a powerful tool that has multiple applications in astrophysics and cosmology. Strong lenses are used to study the dark matter content and distribution in galaxies (Koopmans et al. 2006; Barnabè et al. 2009; Sonnenfeld et al. 2015; Oldham & Auger 2018) and clusters (Richard et al. 2010; Jauzac et al. 2015; Caminha et al. 2019), to study distant galaxies (Marshall et al. 2007; Dessauges-Zavadsky et al. 2015; Swinbank et al. 2015; Cañameras et al. 2017), and to constrain cosmological parameters such as the Hubble constant and the dark energy equation of state from time delay observations (e.g. Suyu et al. 2010, 2014; Sereno & Paraficz 2014; Courbin et al. 2018; Wong et al. 2020; Millon et al. 2020). With the help of strong gravitational lensing of massive clusters, we have also been able to probe galaxy evolution through Ultra-Violet luminosity functions (UV LF) (Atek et al. 2014; Livermore et al. 2017), stellar mass functions (Bhatawdekar et al. 2019; Kikuchihara et al.

2020), and UV slopes (Bhatawdekar & Conselice 2021), well into the epoch of reionisation. Strong gravitational lensing is a rare phenomenon which relies on the chance alignment of a foreground object with a large surface mass density (lens) with a bright background object (source) such as a galaxy, a quasar or a supernova (Kelly et al. 2015). Recently, other lensed sources have also been reported, such as magnified stars and stellar complexes (Welch et al. 2022; Vanzella et al. 2021). Overall, since the discovery of the first gravitational lens (Walsh et al. 1979) only approximately one thousand strong lenses have been confirmed.

Finding strong gravitational lenses is a difficult outlier detection problem. So far, numerous automated algorithms have been developed for the detection of strong lenses in large-scale surveys, for example through the identification of arcs and rings in multiband imaging (e.g. Alard 2006; Marshall et al. 2009; Gavazzi et al. 2014; Sonnenfeld et al. 2018), or through the blended signatures of lens and source galaxies in fibre spectroscopy (e.g. Bolton et al. 2008; Brownstein et al. 2012; Holwerda et al. 2015; Shu et al. 2017; Talbot et al. 2021). With

* e-mail: egarvin@phys.ethz.ch

** e-mail: kruksandor@gmail.com

the latest developments of artificial intelligence, machine learning algorithms, and in particular convolutional neural networks (CNNs), have had an increasing number of applications in astronomy, from galaxy classification (Dieleman et al. 2015; Huertas-Company et al. 2015; Walmsley et al. 2020, 2022) to estimating quantities such as photometric redshifts (Samui & Samui Pal 2017; D’Isanto & Polsterer 2018; Schuldt et al. 2021). Strong lens searches have largely benefited from the use of CNNs (e.g. Bom et al. 2017; Schaefer et al. 2018; Petrillo et al. 2019; Jacobs et al. 2019; Cañameras et al. 2020; Huang et al. 2020). The Bologna strong gravitational lens finding challenge has extensively compared the performance of these methods on simulated data resembling future ground- and space-based imaging surveys such as LSST and *Euclid* (Metcalf et al. 2019). While automated search algorithms are generally highly efficient on real data, they remain affected by false-positives, and they are typically complemented by visual inspection to increase the sample purity (for instance, only $\approx 1\text{--}3\%$ of candidates selected by arc-finders and CNNs are highly-probable lenses; Sonnenfeld et al. 2018; Petrillo et al. 2019).

One distributed method that has been proven successful in the visual identification of strong lenses is citizen science. The general public has been involved in the classification of astronomical data through projects such as Galaxy Zoo (Lintott et al. 2008). The Space Warps project (Marshall et al. 2016) pioneered the crowdsourced identification of strong gravitational lenses in surveys such as CFHTLS (More et al. 2016) and HSC-SSP (Sonnenfeld et al. 2020). Using the Zooniverse framework, Space Warps display images on a web-based interface and ask volunteers whether a gravitational lens is present in the images. To assess the completeness and uncertainty of the classifications, Space Warps measures the performance of each user on a training set of simulated lenses, and weights the individual user contributions based on their ‘skill’.

These various lens search methods typically focus on specific lens configurations. On the one hand, galaxy-scale strong lens candidates identified from unresolved fibre spectra have massive foreground elliptical and Einstein radii limited by the fibre aperture sizes (e.g. Bolton et al. 2008; Brownstein et al. 2012). On the other hand, searches using multiband images from wide-field, ground-based surveys are preferentially selecting candidates with wider image separations ($\geq 2''$ from the lens centre) ensuring robust lens and source deblending, and are therefore spanning both galaxy-scale and more massive group-, cluster-scale foreground halos (e.g. Belokurov et al. 2009; Sonnenfeld et al. 2018; Cañameras et al. 2020). Moreover, the visual grades assigned by strong lens expert and volunteers show large scatter due to the difficulty in distinguishing strong lenses from rings, spirals, mergers, and other contaminants in seeing-limited images (e.g. More et al. 2016; Rojas et al. 2021).

In this study, we employed a crowdsourced approach to detect strong lenses in archival images from the *Hubble Space Telescope* (HST), in order to benefit from the higher angular resolutions, and to cover a broader range of lens and source galaxy types, lens potentials, and multiple image configurations. Instead of showing volunteers postage stamps of galaxies, we displayed cutouts of HST images sufficiently large to contain tens of objects. Although the original project was not designed for the detection of lenses but for the detection of asteroids, we asked the volunteers on Hubble Asteroid Hunter¹ (HAH) to tag possible lenses on the forum of the project, and the science team inspected all the tagged lenses. Several square degrees of

HST imaging have been previously searched for the presence of lenses, for example in the HST AEGIS survey (Moustakas et al. 2007), the GEMS survey (More et al. 2011), the COSMOS survey (Jackson 2008; Faure et al. 2008; Pourrahmani et al. 2018), and over 7 deg^2 of archival observations (Pawase et al. 2014). We extended the systematic morphological selection of strong lenses from the HST archive to a much larger area, without colour, brightness, and redshift cuts, in order to provide a statistically-significant and diverse sample of robust lens candidates for future spectroscopic follow-up and detailed modelling.

The structure of this paper is as follows. In Sect. 2, we present the input data set, and in Sect. 3 we describe the inspection, classification, and light profile fitting. The results and properties of strong lens candidates are given in Sect. 4. Finally, we compare with other search methods in Sect. 5, and we summarise in Sect. 6. Throughout the paper we adopted the WMAP Seven-Year Cosmological parameters (Jarosik et al. 2011) with $(\Omega_M, \Omega_\Lambda, h) = (0.27, 0.73, 0.71)$.

2. Data

We analysed archival HST images from the Advanced Camera for Surveys Wide Field Channel (ACS/WFC) and Wide Field Camera 3 Ultraviolet and Visible (WFC3/UVIS) and Near-infrared (WFC3/IR) channels. These instruments and detectors have the largest field-of-views, thus the highest chance of containing serendipitously observed strong lenses. The observations were taken between 30 April 2002 (when the ACS camera was installed) and 24 April 2020 for ACS/WFC, and between 25 July 2009 (when the WFC3 obtained first light) and 24 April 2020 for WFC3/UVIS. This data is presented in the Kruk et al. (2022) paper. The WFC3/IR images were uploaded later to the project, after the analysis of ACS and WFC3/UVIS data was completed, and consisted of observations taken between 25 July 2009 and 1 June 2020.

The analysis is complete with data taken and publicly available in the HST archives up to 1 June 2020. Observations based on general observer (GO) proposals are available in the HST archive one year after they were taken, therefore the last GO observation analysed were taken before June 2019. HST Snapshot observations are available in the archive immediately after they are acquired and they were analysed up to June 2020. One of the authors, citizen scientist Claude Cornen inspected the data released in the HST archives after June 2020 and found 12 new strong lens candidates. These were not included in the main analysis but presented separately in Appendix C.

In the Hubble Asteroid Hunter (HAH) project, volunteers inspected the single-band HST composite images in PNG format available from the European *Hubble Space Telescope* (eHST) archive (the same images are also available in MAST). These images were created from the FITS images by first applying autoscaling, which scales the image linearly from the 0.5% pixel level to the 99.5% pixel level (using `autoscale=99.5`, which is the default), and then applying a trigonometric `asinh` scaling.²

The composite HST images were obtained by stacking individual HST dithered exposures, processed using the standard HST data processing pipeline by STScI: the exposures were aligned and processed with `DrizzlePac`³ (Gonzaga et al. 2012) for geometric distortion corrections and cosmic ray removal.

² More details on the parameters used can be found at https://hla.stsci.edu/fitstcutcgi_interface.html

³ <https://hst-docs.stsci.edu/drizzpac>

¹ www.asteroidhunter.org

Table 1. HST archival images inspected while searching for strong gravitational lenses in the Hubble Asteroid Hunter project.

HST Instr.	FoV	Scale (''/pix)	Images	Cutouts
ACS/WFC	202'' × 202''	0.05	22 940	91 760
WFC3/UVIS	160'' × 160''	0.04	10 326	41 118
WFC3/IR	123'' × 136''	0.13	12 518	12 518

Notes. The search contains HST observations taken and released between 2002 and June 2020, with exposure times larger than 300s. Images follow the standard HST processing pipeline and are single-band. ACS/WFC and WFC3/UVIS images were divided into 4 equal quadrants (cutouts) in order to maximise the detection of smaller arcs. WFC3/IR images were presented as they are.

In order to optimise the presentation of the images for the visual inspection of citizen scientists, we split the HST ACS/WFC and WFC3/UVIS composite images into four equal parts, of sizes 101'' × 101'' and 80'' × 80'', respectively. For the WFC3/IR images we used the full frame with size 127'' × 137'' for the search. We selected all the composite HST images available in the archive based on the following criteria: an exposure time greater than 300 seconds, and a field-of-view greater than 7 arcmin² to exclude sub-frames (only for ACS/WFC and WFC3/UVIS). Occasionally, the same field was observed multiple times by HST. We showed all the images available, even though observations overlapped in the targeted region of the sky.

In total, 145 396 cutouts were inspected, corresponding to 45 784 unique observations. The inspected images were in grey-scale, without colour information. The total area imaged by HST and inspected in this project is about 27 deg.². This includes the HST Cosmic Evolution Survey (COSMOS; Koekemoer et al. 2007; Scoville et al. 2007), as well as the CANDELS survey (Grogin et al. 2011). The estimate of the total area imaged takes into account the overlap between the HST pointings of the approximately same region of the sky with different instruments and filters. These overlapping observations were nonetheless inspected individually by the volunteers. Details on the images inspected are shown in Table 1.

3. Method

3.1. Visual identification by citizen scientists

We identified gravitational lenses in the Hubble Asteroid Hunter citizen science project (Kruk et al. 2022), launched on 20 June 2019 and which ran until August 2020. The primary purpose of the project was to identify serendipitously observed asteroid trails in HST images while the telescope was observing targeted objects, proposed by astronomers. In total, 11 482 volunteers inspected the 145 396 cutouts, each image being inspected by ten people. The project also had a dedicated forum, *Talk*⁴, where the volunteers could tag cutouts containing interesting objects (with #) and discuss about them.

In contrast to other citizen science projects that are specifically designed to identify strong lenses (such as Space Warps) or projects that have the strong lens classification as part of their workflows (e.g. Galaxy Zoo), Hubble Asteroid Hunter did not provide a classification option for strong lenses. Instead, we

asked the volunteers to specifically tag observations containing strong gravitational lenses on *Talk*, including individual strong lenses (with #gravitational_lens) and clusters of galaxies with arcs corresponding to strong lensing (with #cluster_lens). For training, we provided several examples of strong gravitational lenses, based on previously identified lenses in HST images and targeted lenses, both in the Tutorial and the Field Guide of the project. The science team inspected and assessed all gravitational lenses as the project progressed, instead of analysing the classifications when the project was completed. Finally, it is worth mentioning that some of the citizen scientists on the project who tagged lenses participated in Space Warps and, therefore, have prior training and familiarity with the appearance of strong lenses.

3.2. Visual identification by authors

In total, 2 354 cutouts were tagged as containing individual strong lenses (with #gravitational_lens). Members of the science team (EOG, SK, CC) inspected all the cutouts, selected 417 unique gravitational lens candidates and added them to our catalogue.

The initial catalogue contained the position of the lens, the instrument and filter used. We used the ESASky⁵ portal (Giordano et al. 2018) to retrace the sky coordinates of the lenses in the images. ESASky also reports the objects which appear in previous publications, matching their positions in the HST images with astronomical catalogues and papers from the CDS Simbad database. This eased our work to establish which lenses have been previously published. We also double-checked with other databases such as NED. We classified the objects as being ‘targeted’ (in the case where the strong lenses were the target of the observations, judged based on the corresponding HST proposal), previously ‘published’ (whether they appeared in other publications) or ‘unpublished’. A number of 165 strong lenses were the target of the HST observations, for example by the Sloan Lens ACS Survey (SLACS, Bolton et al. 2008), the CFHTLS-Strong Lensing Legacy Survey (SL2S, More et al. 2012), the CAS-SOWARY survey (Stark et al. 2013), or the BOSS Emission-Line Lens Survey (BELLS, Shu et al. 2016). These targeted lenses were excluded from our analysis. The remaining 252 strong lenses were not the primary targets of the HST observations. We searched for these objects on ESASky, NED, and enquired with the 96 Principal Investigators of these HST observations whether they appear in previous publications. 54 have been previously identified and appear in other publications. Hence, we are left with 198 unknown, new lens candidates distributed on the sky according to Fig. 1.

Three members of the science team (EOG, SK, CC) assigned a grade to each lens, based on: the morphology, the shape of the source image and the quality and availability of a colour image. We discussed each object and agreed on a final grade. The criteria used for the classification are inspired by the convention of More et al. (2016), and define the likelihood of each object to be a strong lens. Grades A are almost certainly lenses. They are the most promising candidates based on the configuration of the lens, and the morphology in the colour- or grey-scale images. Their identification is based on the presence of an image and counter image, and on a clear colour separation between the lens and image (if colour information was available). Grades B are highly probable lenses. These are also high-quality candidates showing probable lensing features, but with typically fewer clear

⁴ <https://www.zooniverse.org/projects/sandorkruk/hubble-asteroid-hunter/talk>

⁵ <https://sky.esa.int/>

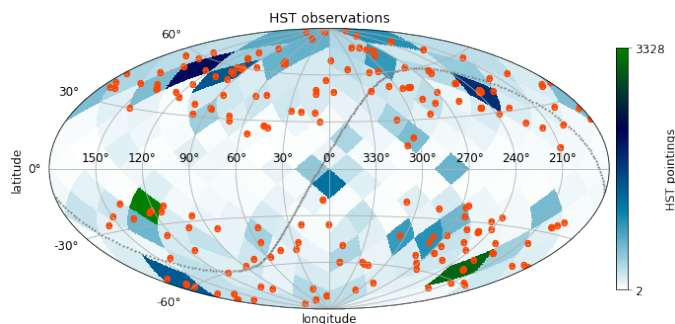


Fig. 1. Map in galactic coordinates showing the sky position of the newly discovered lenses serendipitously observed with HST (red points), over the densities of the parent sample of HST pointings analysed in the HAH project (in tiles of ~ 215 deg.² each). The sky distribution of the HST observations with strong lens candidates is roughly isotropic, excluding the Galactic Plane. The grey dotted line represents the ecliptic.

and bright counter-images, and less colour information available than grades A. Their confirmation requires spectroscopic follow-up or lens modelling. Grades C are maybe lenses. These possible strong lens systems mostly have single arcs without clear counter-images. They are more difficult to distinguish from non-lens contaminants, and some could be tidal tails, compact groups, or weakly lensed arcs.

We further classified the morphology of the source images into ‘Arc’, which is the most common class, ‘Double’ (two images), ‘Triple’ (three images), ‘Quad’ (four images), and ‘Ring’ or ‘Cross’ for the rarest Einstein ring and Einstein cross configurations. Additionally, we classified the morphology of the lenses into ‘elliptical’, ‘disc’ and ‘edge-on disc’.

3.3. Measuring the arc radii

A measurable parameter for the strong lenses in our sample is the arc radius, which can be used as a proxy for the Einstein radius. For the strong lenses made of a single arc, we measured the radius of the circle centered on the brightest pixel of the lensing galaxy and tangent to the arc, using both the DS9 and the Aladin ‘circle’ tool. For the other configurations, we drew a circle, or the best matching ellipse, as a substitute for the outer tangential critical curve in the lens plane and measured its radius.

3.4. Galfit modelling of the lenses

In this subsection, we describe the fitting process using GALFIT (Peng et al. 2002) to determine the parameters of the lenses: the magnitudes, effective radii, axis ratios, and position angles. These parameters are important for future tasks, such as lens modelling and source reconstruction, which are not covered in this work.

We fitted a total of 252 lenses with GALFIT, including the 198 previously unknown systems, and the 54 which were already identified and published, as discussed above. We used the sky position of the lenses to create cutouts with square sizes of $10''$, centered on the objects, from the single-band composite HST images available in eHST. If multiple bands were available, we used the reddest band available, which was F814W in the majority of cases. The band used for fitting is shown in Table A.1 and Table A.2.

To ensure that only the lenses are fitted, we masked out the other objects in the cutouts, including the arcs and any other

background image, with SExtractor (Bertin & Arnouts 1996). We created images of the HST Point Spread Function (PSF) using TinyTim (Krist 1995), for the band corresponding to each image and the position of the object in the corresponding image, which we use for the fitting. We fitted the lenses with a single Sérsic profile (Sérsic 1968) described by the following equation:

$$\Sigma(r) = \sum_e \exp \left\{ -k \left[\left(\frac{r}{r_e} \right)^{\frac{1}{n}} - 1 \right] \right\}, \quad (1)$$

where $\Sigma(r)$ is the surface brightness at radius r , r_e is the half-light radius, \sum_e is the effective surface brightness, k is a normalisation coefficient and n is the Sérsic index. As starting parameters, we used a magnitude of 20, an axis ratio of 0.9, and an effective radius of $0.5''$.

We used a fixed De Vaucouleurs profile ($n = 4$) for the majority of the lenses (243 galaxies), which we classified as being elliptical galaxies. We fitted the remaining 23 galaxies which we classified as being discs with an exponential Sérsic index ($n = 1$). We note that in the case of group-scale lenses, we fitted multiple galaxies which we deemed to be the lenses, hence the total number of galaxies fitted is higher than the number of strong lens candidates. We show the GALFIT models and residuals of the A grade lenses in Fig. B.1 and Fig. B.2.

To determine the magnitudes, we calculated the zero points based on the quantities provided in the FITS headers, using⁶:

$$m_{AB} = -2.5 \log_{10}(F) - 2.5 \log_{10}(\text{PHOTFLAM}) - 2.5 \log_{10}(\text{PHOTPLAM}) - 2.408, \quad (2)$$

where PHOTFLAM is the inverse sensitivity and represents the scaling factor necessary to transform an instrumental flux in units of electrons per second to a physical flux density, and the PHOTPLAM is the pivot wavelength provided in the FITS header and used to derive the instrumental zero point magnitudes. For consistency, we also measured the magnitudes of the lenses with SExtractor (mag_{AUTO} and mag_{ISO}). We compare the magnitudes estimated with GALFIT and SExtractor in Figure B.3 and find that the measurements are consistent between the different methods.

4. Results

We present the results on the 198 newly identified lens candidates (which we henceforth call ‘discovered’) in Table A.1, and on the 54 previously published lenses (which we henceforth call ‘rediscovered’) in Table A.2. The lenses in the tables are grouped by grades, and postage stamps of the Grade A, Grade B, and Grade C lenses are shown in Figures 2, 3, and Figure 4, respectively. In the tables we provide the IAU name, the RA and Dec coordinates of the candidate, the instrument corresponding to the HST observation in which the lens was found, and the filter used for light fitting. We also provide our measurements of the arc radii, r_{arc} , as well as the magnitude, the effective radius, r_e , the axis ratio, q , and the position angle, PA, measured using GALFIT. We also list our classification into Arc, Double, Ring, and Quad configurations.

While the sample mainly consists of galaxy-galaxy lens configurations, some of the lens galaxies may be part of a cluster, in which case the strong lensing effect can be enhanced by the mass distribution of the cluster. In addition, the presence of a

⁶ <https://www.stsci.edu/hst/instrumentation/acs/data-analysis/zeropoints>

structure along the line-of-sight, either in front or behind the main lens plane, will also perturb the light deflection. Firstly, we identify the lens candidates that are associated with known foreground galaxy clusters (from, e.g. MACS, Abell, RELICS catalogues) using the target name of the HST observations. Secondly, to get a more comprehensive overview of the lens candidates located in possible cluster fields, we also cross-match with the positions of cluster candidates selected (1) from SDSS DR8 data with the redMaPPer algorithm (the SDSS catalogue from Rykoff et al. 2016), and (2) in the footprint of DESI legacy imaging surveys based on a photometric redshift clustering analysis (DR8, Zou et al. 2021). Both surveys cover a significant fraction of the line-of-sights towards our HAH lenses. We use a maximal cross-match radius of $3'$ corresponding to ≈ 1 Mpc at $z \sim 0.5$. Tables A.1 and A.2 indicate whether each lens matches the position of a cluster, and Table A.3 gives additional information on the cluster names and angular separation. In total, 124 out of the 198 new lens discoveries and 32 out of the 54 rediscoveries are within $3'$ from the centroid position of a candidate or confirmed cluster.

Finally, we search for redshifts available for the lens galaxies. We provide either the photometric or spectroscopic redshift, if available, retrieved from NED or from the SDSS-IV DR16 (Ahumada et al. 2020). Additionally, the last column of Table A.2 lists the reference papers for the candidates previously published.

4.1. Distribution of lens properties

In the previous sections, we described how the gravitational lenses were found and reported into discovered and rediscovered lenses and we explained how we fitted them in order to retrieve the lens parameters. In this subsection, we describe the results, namely the distributions of properties such as arc radii, and lens redshifts, magnitudes, and effective radii. The properties are grouped by either discovered or rediscovered lenses, and by visual grade.

In Figure 5, we plot the distribution of photometric and spectroscopic redshifts from SDSS and NED for the lens galaxies for which this information was available. The median redshift of our sample is $z = 0.41$, and the distribution is skewed to higher redshifts, up to $z = 1.3$. The discovered and rediscovered lenses show similar distributions, while Grade A lenses are, on average, at lower redshifts compared to Grade B or C. The redshift distribution of the lenses in our sample is also broadly consistent with the lens galaxy redshifts from previous ground-based searches (e.g. Bolton et al. 2008; Stark et al. 2013).

Figure 6 shows the distribution of magnitudes over all instruments and filters. We find that the magnitude of reported objects are distributed around an average value of $m = 20.6$. Although our sample contains lenses observed with WFC3/IR, which are typically brighter, our average magnitude is 1.3 magnitudes fainter than the average magnitude $m = 19.3$ of the sample of lenses found by Pawase et al. (2014) in a previous search in ACS images. The violin plots in Figure 6 show that the magnitudes of the discovered lenses are fainter than those of rediscoveries ($m = 20.8$ vs. $m = 20.1$). Indeed, the faintest lens found has a measured magnitude of $m = 26.4$ compared to $m = 23.6$ in the rediscovered group. Moreover, a quarter of the rediscovered objects were detected above $m = 21$, while a quarter of the new discoveries have a magnitude above $m = 21.9$. Interestingly, Grade C lenses are brighter than Grade B or Grade A, showing that we did not assign the grade based on brightness, but on the morphology. It is important to note that the magnitudes are plotted

together for both the ACS and WFC3 instruments and some are measured in different filters (see Table A.1 for the filters used).

As for the arc radii of the lenses, the distribution is right skewed, with a median of $r_{\text{arc}} = 1.58''$ and a mean of $r_{\text{arc}} = 1.94''$. Although it is consistent with the distribution of arc radii presented in Pawase et al. (2014), we notice from the plot on the left in Figure 7 that our detected lenses include more extreme arc radii than their sample. Indeed, a few of the newly discovered arc radii range up to $r_{\text{arc}} = 4.5''$, which corresponds to group-scale lenses. In addition, for our newly discovered lenses, the median arc radius is $r_{\text{arc}} = 1.23''$ and the smaller arcs we find have a radius of only $r_{\text{arc}} = 0.33''$. This shows a relative improvement in finding smaller separation arcs in comparison to previously reported lenses (in the rediscovered group), for which median $r_{\text{arc}} = 1.67''$ and the smallest arcs have radii $r_{\text{arc}} = 0.61''$. Furthermore, a quarter of the rediscovered objects were found to have $r_{\text{arc}} \leq 0.88''$ while a quarter of our newly discovered objects have $r_{\text{arc}} \leq 0.82''$. This observed difference in the median arc radii and their distribution (shown in the central plot in Figure 7) indicates that citizen science as a strong lens detection method has a potential to unveil arcs with smaller angular separations from the source. This potential deserves to be further investigated and quantified in future studies.

The distributions of lens galaxy effective radii (Figure 8) show a median $r_e = 0.66''$ and are consistent across discovered and rediscovered groups, as well as with the distribution in Pawase et al. (2014).

Finally, the mosaic plot from Figure 9 shows a visual representation of a proportion test on the contingency table of the grades assigned by members of the science team (EOG, SK, CC) to the discovered and rediscovered lenses. We can see that the C grades are relatively larger in proportion than the B grade and A grade lenses in the discovery group, while the A grades are more frequent than both the B and C grades in the rediscovery group.

Overall, the results we presented in this sub-section highlight the interest and importance of the contribution of citizen scientists and detection by human eye in order to continuously cross validate and improve the performance of classical algorithms.

4.2. Properties of the high-quality candidates

The morphological search conducted in this paper results in strong lenses with high diversity of image configurations and lens potentials, and their future spectroscopic follow-up and detailed modelling will enable a range of valuable studies. In Sect. 4.2.1, we illustrate possible applications with the highest-quality, newly-discovered, grade A candidates in Fig. 2. In Sect. 4.2.2, we further describe the lensing configurations and we highlight the properties of few individual lenses.

4.2.1. Prospects for scientific studies

Strong lenses with distant, isolated foreground galaxies are promising to improve our understanding of the total mass-density slope, γ_{tot} , of early-type galaxies. While it is firmly established that γ_{tot} is nearly isothermal at low redshift (e.g. Treu & Koopmans 2004; Koopmans et al. 2006; Cappellari et al. 2015), its evolution at $z < 1$ remains debated, with strong lensing studies suggesting a mild increase from $z \sim 1$ to $z \sim 0$ (Koopmans et al. 2006; Bolton et al. 2012; Sonnenfeld et al. 2013; Li et al. 2018), and Jeans dynamical modelling and cosmological simulations favouring nearly constant γ_{tot} over this period (e.g. Wang et al. 2019; Derkenne et al. 2021). Measurements are mainly

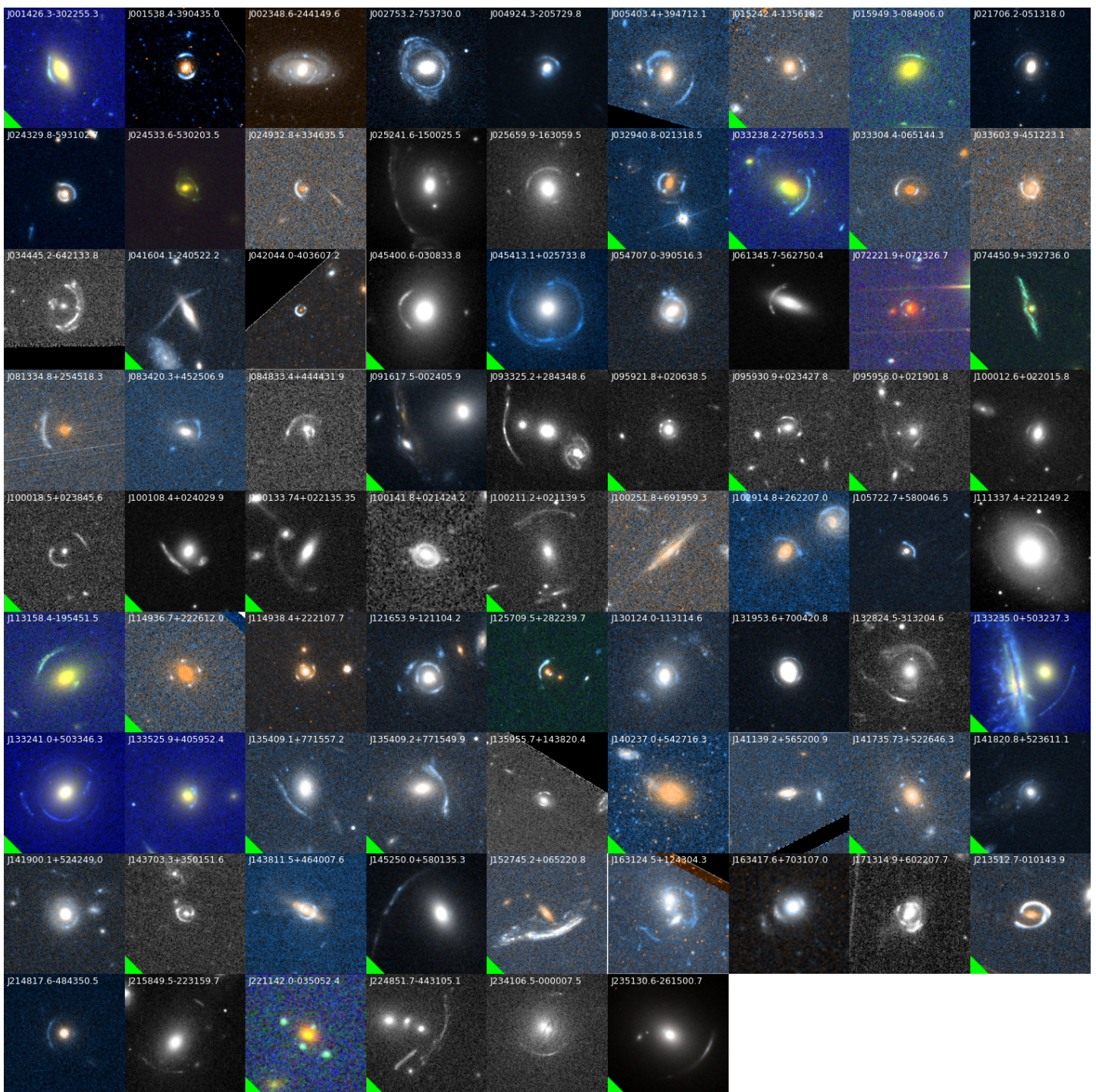


Fig. 2. The 78 grade A HAH lenses identified in this study, with green triangles indicating the 33 ‘rediscovered’ lenses. The lenses are indicated using the sequence part of their name. Postage stamps are $10'' \times 10''$. The orientation of the images is North up and East is to the left.

restricted to early-type galaxies at $z \lesssim 0.6$ and need to be extended to higher redshifts in order to further test galaxy evolution models. Systems with the most distant, isolated deflectors (e.g. HAH J083420.3+452506.9 at $z_{\text{spec}} = 0.65$) are very useful in that regard, as well as future spectroscopic follow-up of lenses with $z_{\text{phot}} > 0.6$ (e.g. HAH J005403.4+394712.1, HAH J125709.5+282239.7).

Double source plane lenses are beneficial to infer tight constraints on the foreground total mass-density profiles (e.g. Tu et al. 2009). Multiple images covering different angular separations from the lens centre, as for instance in HAH

J121653.9–121104.2, and HAH J132824.5–313204.6, break parameter degeneracies in the lens models. Together with multi-band photometry or stellar kinematic measurements, such lensing configurations enable to characterise the lens dark-matter distributions. Moreover, when the background sources lie at distinct redshifts, measuring the two Einstein radii can provide valuable and independent constraints on the equation of state of dark energy (Collett et al. 2012). Only a handful of double source plane lenses are known to date (e.g. Gavazzi et al. 2008; Tanaka et al. 2016), and in our sample, HAH J002753.2–753730.0 and HAH J132824.5–313204.6 are good candidates. The former

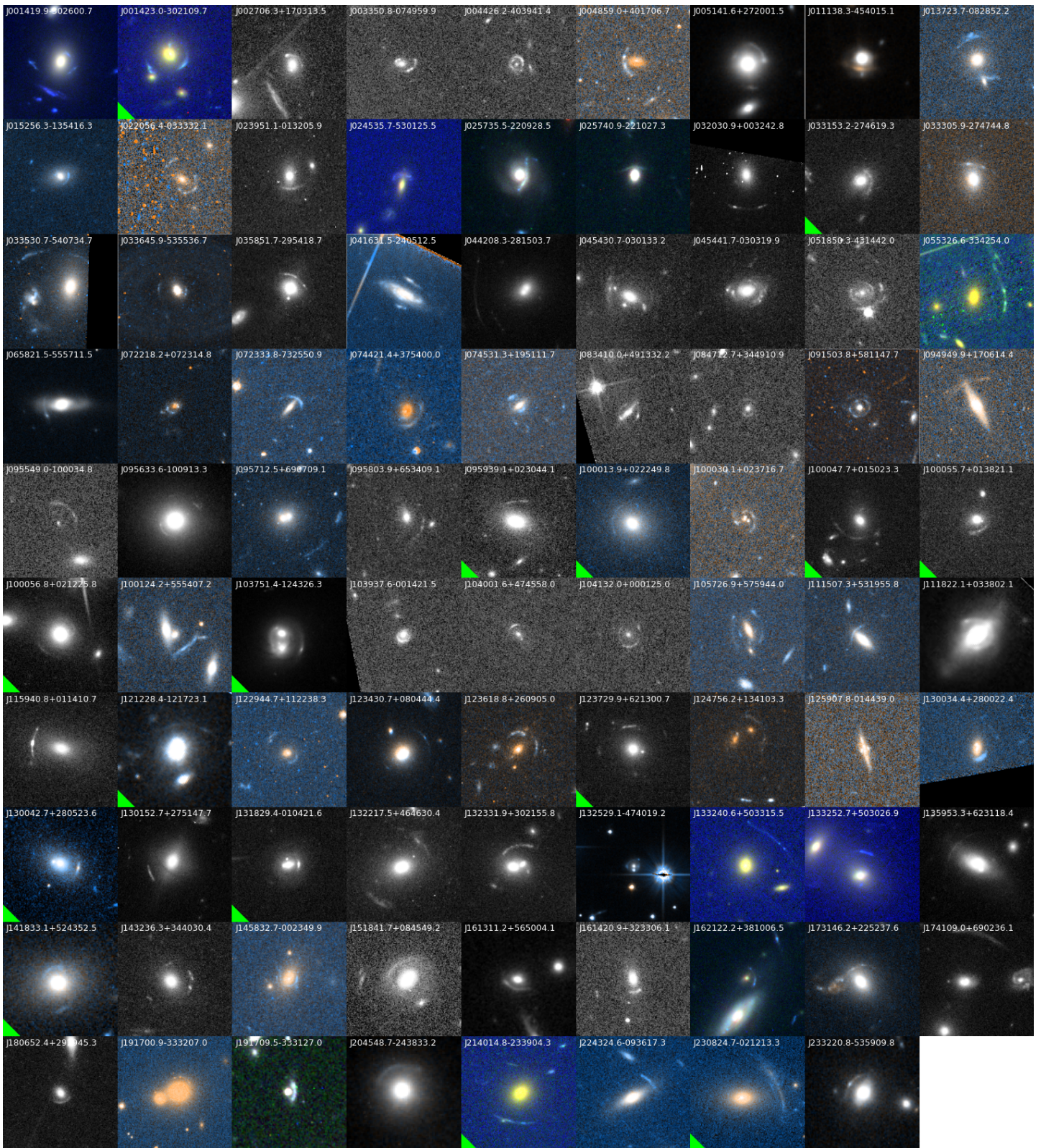


Fig. 3. The 89 grade B HAH lenses identified in this study, with green triangles indicating the 15 ‘rediscovered’ lenses. The lenses are indicated using the sequence part of their name. Postage stamps are $10'' \times 10''$. The orientation of the images is North up and East is to the left.

shows two opposite blue, thin arcs surrounding a foreground elliptical galaxy, and a broad fuzzy ring that could be a distinct background source. Possible applications to cosmology make these strong lenses well-suited for spectroscopic follow-up.

In addition, systems with isolated lens galaxies and bright, extended, and structured lensed arcs are typically prioritised to search for the presence of foreground dark-matter sub-halos and line-of-sight halos (e.g. Vegetti & Koopmans 2009; Ritondale et al. 2019). Due to their arc surface brightness distribu-

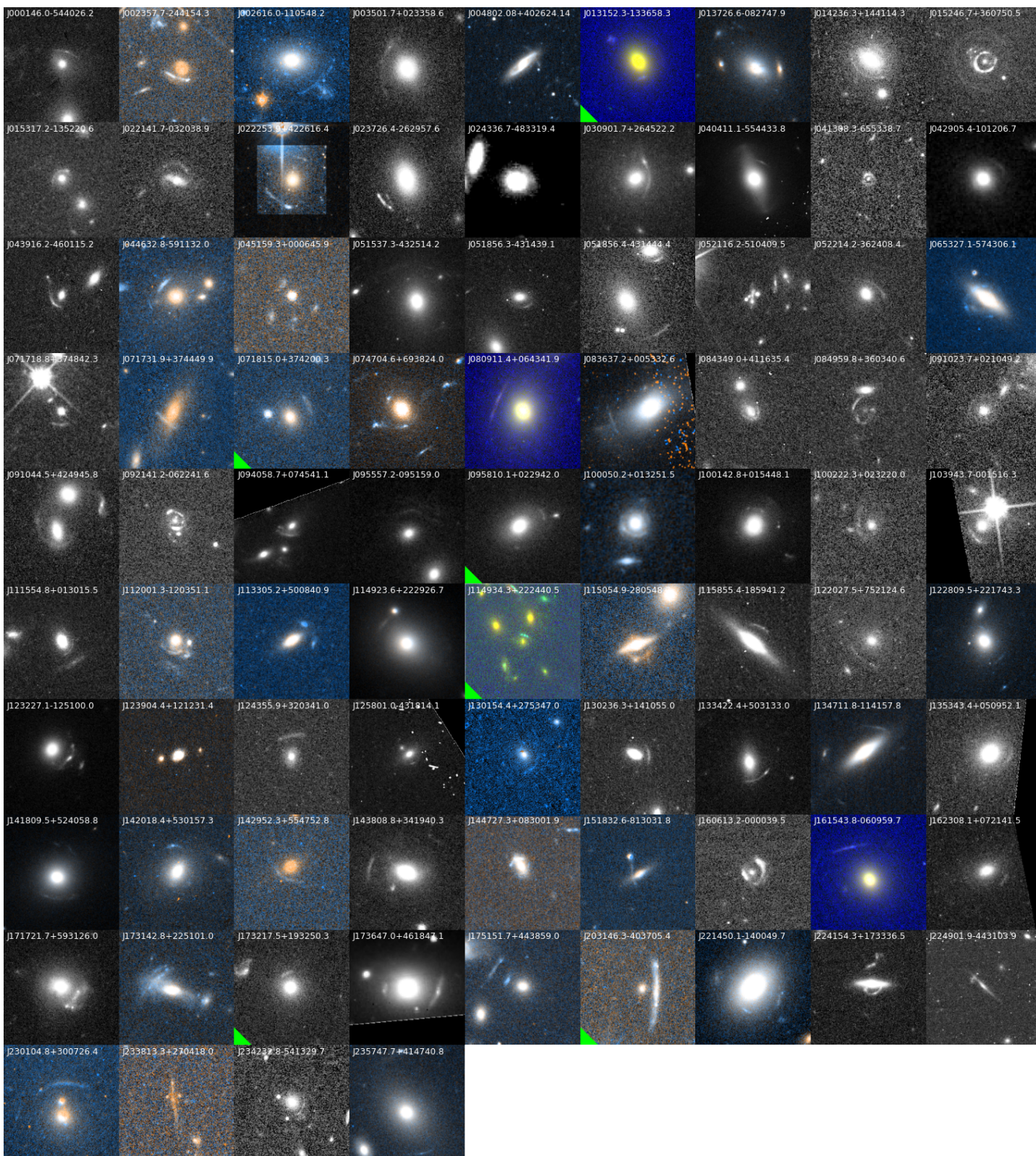


Fig. 4. The 85 grade C HAH lenses identified in this study, with green triangles indicating the 6 ‘rediscovered’ lenses. The lenses are indicated using the sequence part of their name. Postage stamps are $10'' \times 10''$. The orientation of the images is North up and East is to the left.

tions, HAH J025659.9–163059.5, HAH J105722.7+580046.5, and HAH J113158.4–195451.5 have the potential to put valuable constraints on foreground mass perturbations.

4.2.2. Strong lensing configurations

While Tables A.1 and A.3 indicates the presence of galaxy clusters along the lines-of-sight towards several candidates, the image separations and the morphologies in Fig. 2, 3 and 4 show that in fact, most have galaxy-galaxy strong lens configurations.

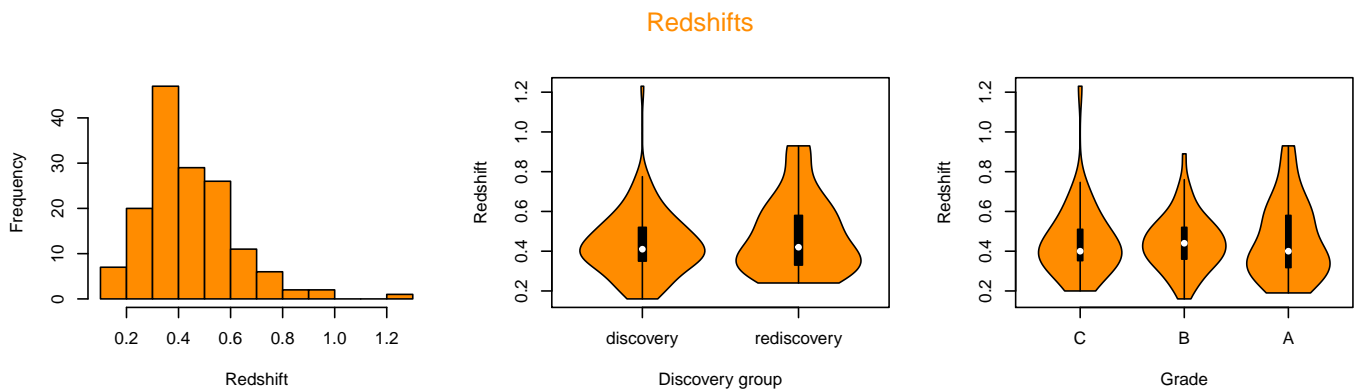


Fig. 5. The first sub-figure on the left shows a histogram distribution of the redshifts retrieved with SDSS and NED (both photometric and spectroscopic). The middle sub-figure uses a violin plot to show the respective empirical distributions of discovered and rediscovered lenses. The right sub-figure shows violin plots per grade groups. The violin plots were fitted using a Gaussian kernel, with the software R.

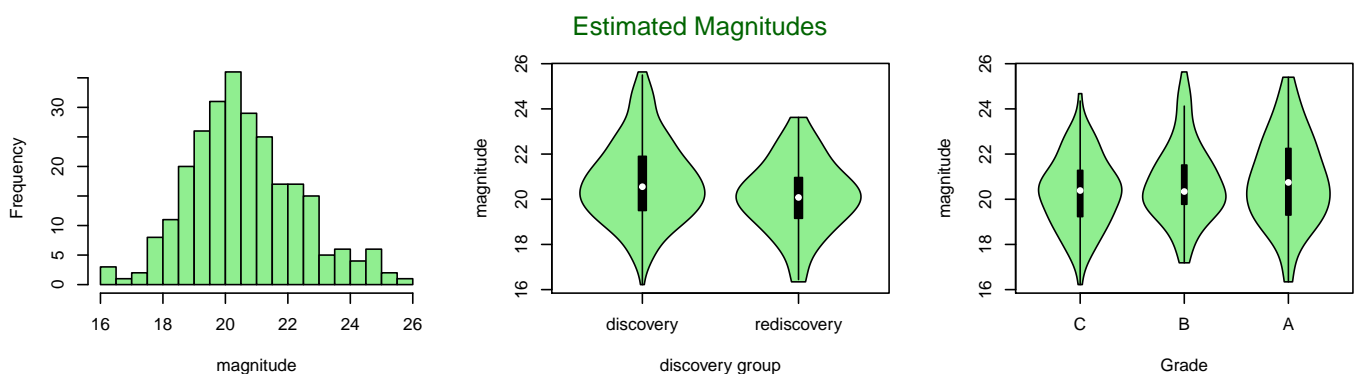


Fig. 6. The left panel shows a histogram distribution of the apparent magnitudes as measured with GALFIT (in the filter mentioned in Table A.1 and Table A.2). The middle panel shows violin plots as the respective empirical distributions of discovered and rediscovered lenses. The right panel shows empirical distributions of magnitudes for each grade group.

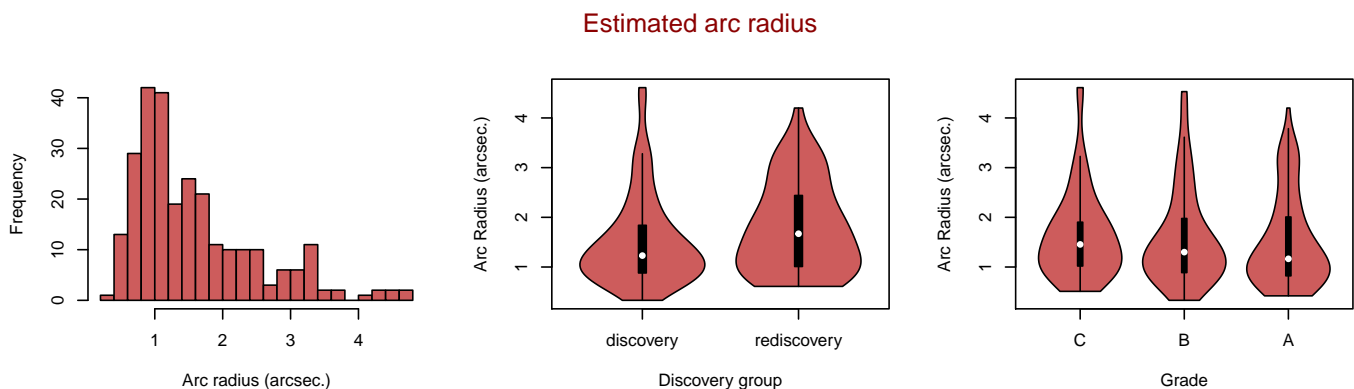


Fig. 7. The first sub-figure on the left shows a histogram distribution of the measured arc radii. The middle sub-figure uses violin plots to show the respective empirical distributions of discovered and rediscovered lenses. The right sub-figure shows empirical distributions of arc radii per grade groups. The distributions are all skewed to the right.

In particular, the light deflection is dominated by a single member or line-of-sight galaxy for 20 out of 21 newly-discovered grade A with foreground confirmed or candidate clusters. Only HAH J025241.6–150025.5 shows an extended arc and is located within $0.5'$ from the centroid position of a cluster candidate listed in Zou et al. (2021). Three grade A have $r_{\text{arc}} > 3''$, suggesting a major contribution from an extended group- or cluster-

scale mass component to the external convergence and shear and, for instance, HAH J093325.2+284348.6 comprises a compact group of three foreground galaxies. These three systems are nonetheless absent from our compilation of cluster candidates selected from shallower ground-based imaging. In addition, Fig. 2 shows a compact group at $z_{\text{spec}} = 0.1895$ towards HAH J234106.5–000007.5, but this system has smaller image

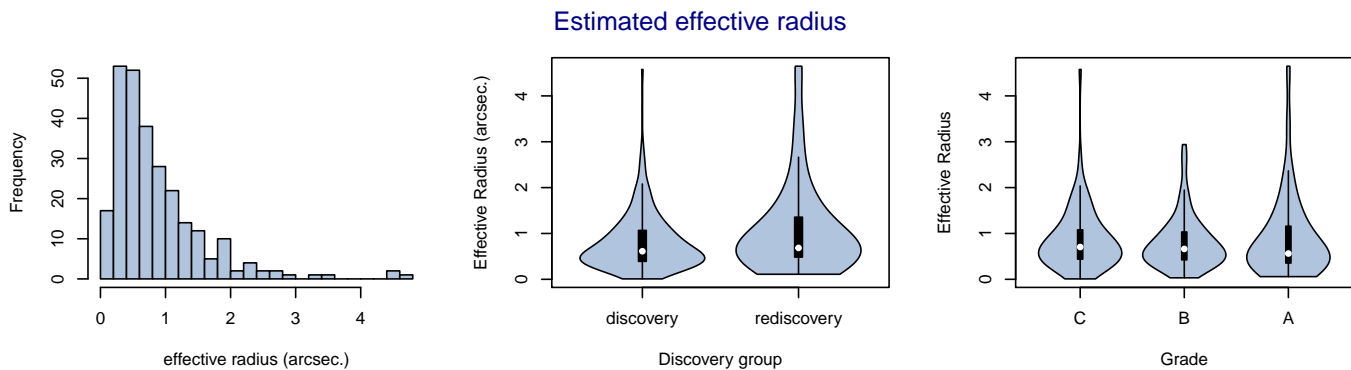


Fig. 8. The first sub-figure on the left shows a histogram distribution of the effective radii measured with GALFIT. The middle and right sub-figure shows empirical Gaussian kernel distributions of lenses, separated per discovery (middle panel) and per grade (right panel).

Relative grade proportions per group

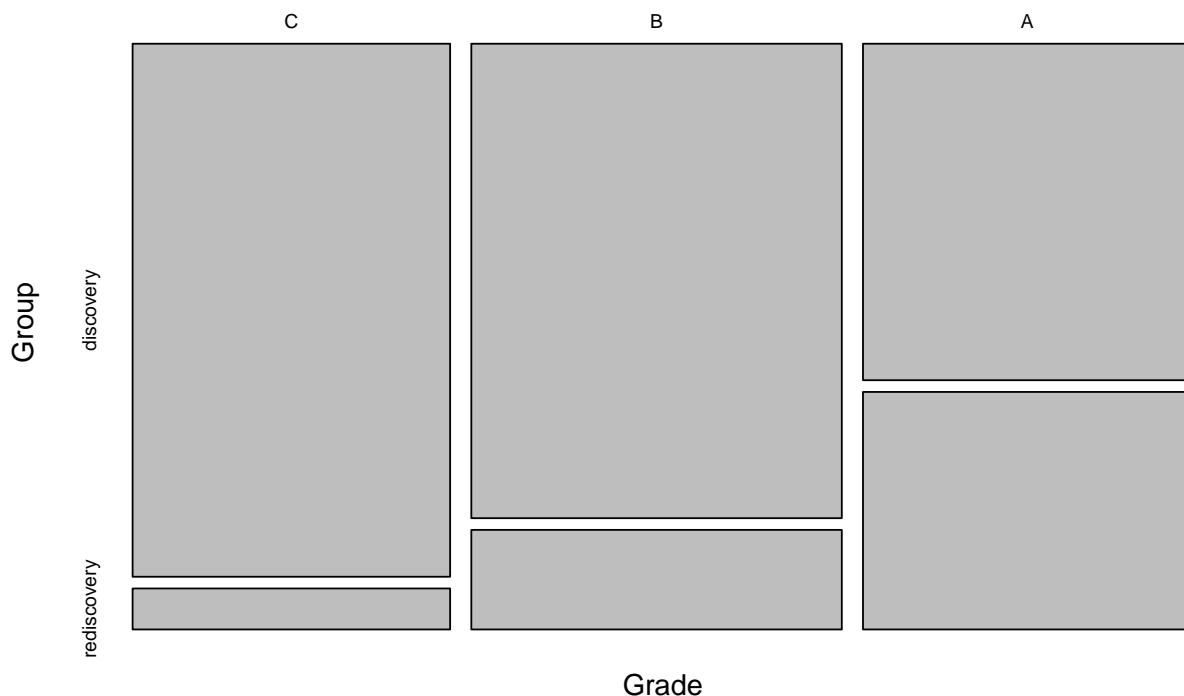


Fig. 9. The mosaic plot shows the discovery groups and grades in a visual representation of a contingency table. The widths of the stacked boxes represent the fraction of each grade in the sample, while the heights of the boxes represent the proportion per discovery group. All the grades have been assigned by three members of the science team (EOG, SK, CC) after consensus following the individual evaluations. We observe that in the discovery group, we have a higher fraction of C grades compared to A grades. In the rediscovery group, there is a higher fraction of A grades compared to both B and C grades. Hence, the mosaic plot indicates that, overall, our grading scheme is rather conservative towards newly discovered lenses.

separation ($r_{\text{arc}} \simeq 2.3''$), and the associated candidate from Zou et al. (2021) is $> 2'$ away. Towards the low-end of the image separation distribution, several grade A candidates have very compact configurations with sub-arcsec Einstein radii, as best shown by HAH J042044.0–403607.2 with $r_{\text{arc}} \simeq 0.4''$. This extends current samples of compact, galaxy-scale strong lenses

(e.g. SLACS, Bolton et al. 2008), and illustrates the new discovery space that will be unlocked by the *Euclid* survey with comparable, high-resolution imaging over $\simeq 15,000 \text{ deg}^2$.

The sample contains a majority of extended, distorted arcs and rings, which are much less ambiguous than configurations with more compact lensed sources. HAH J001538.4–390435.0,

HAH J005403.4+394712.1, and HAH J024329.8–593102.7 are examples of systems with pairs of blue lensed arcs while HAH J061345.7–562750.4 shows a single, but particularly elongated arc, and HAH J033603.9–451223.1 or HAH J100141.8+021424.2 exhibit near-complete Einstein rings. The difficulty in identifying doubles is coming from their similarity with compact groups and other non-lens contaminants in the grey-scale HST images seen by volunteers during the first stage of the classification. HAH J100251.8+691959.3 is the only new grade A candidate firmly identified as a blue, doubly-imaged source from the inspection of colour images by the science team. HAH J002348.6–244149.6 also shows compact images, but in a quadruple configuration.

In terms of morphological types, our sample contains interesting classes of foreground lens galaxies. While traditional selection methods are mainly restricted to massive elliptical lens galaxies, the angular resolution reached from space is key to extend to less common lens galaxy types, and to asymmetric, or more exotic configurations which are particularly difficult to identify from the ground. Firstly, the new A grade HAH J002348.6–244149.6 comprises a moderately inclined lens spiral galaxy with a bright, blue point-like image in the north and three images distributed evenly along a southern thin arc. This system extends the small number of known spiral deflectors with prominent discs (see also, the SWELLS survey, Treu et al. 2011) and, due to the relative positions of multiple images, its modelling has the potential to tightly constrain the galaxy bulge mass. Secondly, HAH J100251.8+691959.3 and HAH J143811.5+464007.6 show edge-on disc galaxies with $r_{\text{arc}} \approx 0.6\text{--}0.7''$. Thirdly, the flexibility of the crowdsourced classification is demonstrated by the complex structure of the previously published A grade lens HAH J133235.0+503237.3 (Ragozzine et al. 2012). A background galaxy is lensed into a thin elongated arc by a spectacular foreground environment, where an edge-on jellyfish galaxy and nearby ellipticals are embedded within the merging cluster A1758N $z = 0.279$ (Ebeling & Kalita 2019).

Most candidates with SDSS spectroscopic follow-up have large image separations (e.g. HAH J111337.4+221249.2), which limits the contribution from the lensed sources to the emission collected in the $2''$ diameter aperture fibres. This limits the number of candidates with spectroscopic redshift measurements for both the lens and source. We nonetheless inspected the SDSS spectra of all grades A, and identified multiple emission lines inconsistent with the lens redshift of 0.6495 for HAH J083420.3+452506.9 ($\sigma_* = 269 \pm 48 \text{ km s}^{-1}$). Our estimate $r_{\text{arc}} \approx 0.6''$ suggests that the lens and source galaxies are blended in the SDSS spectrum, and that the background source is a star-forming galaxy with detections of CIV- $\lambda 1549$, HeII- $\lambda 1640$, OIII- $\lambda 1664$, and CIII]- $\lambda 1908$ emission lines (see Fig. 10). The [OII]- $\lambda 3727$ doublet is also tentatively detected at 9942.6 \AA and 9949.47 \AA . By fitting the smoothed spectrum, we inferred a probable source redshift of ≈ 1.667 . Higher signal-to-noise ratios are nonetheless needed to confirm this estimate.

5. Discussion

5.1. Citizen science for lens finding

Previous strong lens searches have relied on dedicated citizen science projects, the most well-known example being the Space Warps project (Marshall et al. 2016), which was also built within the Zooniverse framework. Space Warps has demonstrated that the visual inspection of volunteers is an efficient data mining

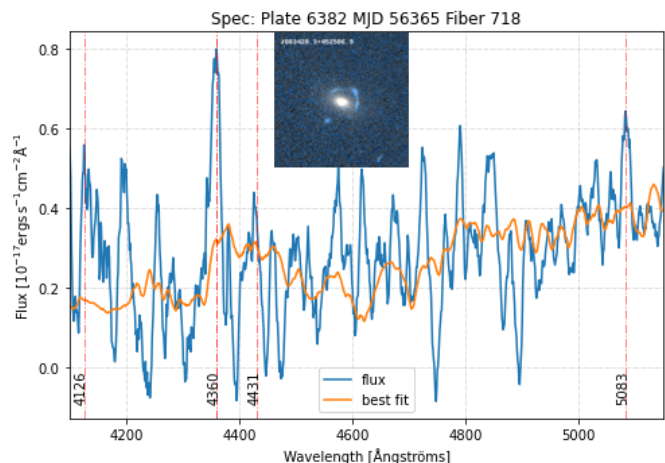


Fig. 10. BOSS spectrum of the newly-discovered grade A candidate HAH J083420.3+452506.9 showing multiple emission lines inconsistent with the spectroscopic of the foreground early-type galaxy of 0.6495. The blue and orange lines show the observed spectrum and the best-fit SDSS model for the central lens galaxy, respectively. The vertical lines mark the positions of the CIV- $\lambda 1549$, HeII- $\lambda 1640$, OIII- $\lambda 1664$, and CIII]- $\lambda 1908$ emission lines at $z \approx 1.667$, from left to right.

tool for strong lenses. It has been successfully applied to the CFHT Legacy Survey finding 29 promising (and 59 total) new lens candidates (More et al. 2016). More recently, Sonnenfeld et al. (2020) used a dedicated algorithm, YATTALENS (Sonnenfeld et al. 2018) and a citizen science approach on Space Warps to find lenses in the HSC survey, finding 14 definite lenses (grade A), 129 probable lenses (grade B), and 581 possible (grade C) lenses in total. Citizen science approaches have also been implemented for lens modelling (Küing et al. 2015).

Our citizen science project and Space Warps employ different approaches for the inspection of images. Space Warps shows to the volunteers postage stamps of objects, generally pre-selected with some criteria (for example, objects within a redshift and mass range), in order to maximise the chances of detecting strong lenses and minimise the required volunteer effort. They also inserted simulated lenses in order to calibrate the response of the volunteers and measure the completeness.

In contrast, in our project we show large fields-of-view to the volunteers and ask them to tag on ‘Talk’ if they think the image contains a strong lens. While the Space Warps approach provides a measure of completeness, which is difficult to assess in our case, our project provides an unbiased search for strong lenses (since our images were not pre-selected with some criteria), being able to find more exotic/interesting lenses. Sonnenfeld et al. (2020) also mention in the Space Warps project that there were candidates flagged on the ‘Talk’ section of the Space Warps project that would have otherwise been missed using the main workflow of the project.

Additionally, using large fields-of-view (corresponding to $80'' \times 80''$ or larger) allowed us to explore the HST images much faster than showing individual postage stamps of galaxies. Finally, this is the first time the HST images are explored with a citizen science approach, showing the benefit of asking volunteers to inspect space-based images spanning decades in time.

5.2. Comparison to previous HST studies

Previous visual searches for strong gravitational lenses in HST images has been undertaken by Faure et al. (2008) and Jackson (2008) in the 1.64 deg² COSMOS field and Pawase et al. (2014) on 7 deg² of archival ACS/WFC I-band and WFC3/IR in the near-infrared channel F160W HST images taken until 31 August 2011. Additionally, Pourrahmani et al. (2018) trained a convolutional neural network on classifications by Faure et al. (2008) to identify strong lenses in COSMOS.

In a first dedicated exploration of the COSMOS field, Faure et al. (2008) identified 67 low-grade strong galaxy-lens candidates with 20 of them displaying multiple images or obvious arcs. Their searches were limited to massive early-type lenses only with arcs at radii smaller than 5". Jackson (2008) visually explored all galaxies in COSMOS that are brighter than 25 mag finding two more certain and one probable lens, in addition to the lenses presented in Faure et al. (2008). Pourrahmani et al. (2018) identified 11 more candidate strong lenses in COSMOS, using the automated LensFlow machine learning algorithm. Nine of the lenses we identified were reported in previously lens searches in COSMOS (shown in Table A.2). We recover two more lenses in COSMOS (HAH J100142.8+015448.1, HAH J100222.3+023220.0) which were not previously reported.

In the only other archival search for gravitational lenses in HST images, Pawase et al. (2014) explored 7 deg.² ACS/WFC I-band and WFC3/IR F160W HST images taken until 31 August 2011. They found 40 lens candidates in ACS and 9 in the WFC3/IR images. Even though the images we inspected overlap, we only recovered seven strong lenses (four secure cases) in common between the two studies (see Table A.2). There are 12 cases labelled by Pawase et al. (2014) as secure lenses not recovered in this study. In addition, eight of our grade A lenses (HAH J054707.0-390516.3, HAH J145250.0+580135.3, HAH J045413.1+025733.8, HAH J171314.9+602207.7, HAH J005403.4+394712.1, HAH J084833.4+444431.9, HAH J025241.6-150025.5, HAH J100108.4+024029.9) observed by HST before 31 August 2011 were not recovered by Pawase et al. (2014). This relatively low overlap between the two samples is due to the different approaches: postage stamp inspection by experts (in the case of Pawase et al. 2014) and large cutout inspection by an army of citizen scientists (in our case). It also shows the difficulties in the visual inspection searches of strong lenses, as studies differ in how liberal or conservative are in the definition of lenses.

5.3. Comparison to automated lens search

Strong lens candidates in this paper were drawn from the largest and most extensive search of 27 deg² archival HST images taken until June 2020. The selection is purely based on morphological criteria, and relies on the systematic inspection of HST images without colour, brightness, or redshift pre-selections. This type of crowdsourced classification is expected to recover the majority of lensing configurations, as long as multiple images are spatially-resolved (see, e.g. Sonnenfeld et al. 2020), and Sect. 4 illustrates that candidates indeed cover a large variety of lens and source galaxy types, image multiplicity and angular distributions, including exotic lenses.

This approach differs from automated searches in several aspects. Firstly, robots are generally run on wide-area, ground-based imaging and spectroscopic surveys, and focus on massive foreground early-type galaxies due to their high lensing cross-section (e.g. Oguri & Marshall 2010), and to their smooth light

distributions and typical rest-frame optical spectra facilitating the identification of signatures from background lensed images. This allows to deal with memory limitations but restricts automated classifications to relatively small pre-selected samples (Bolton et al. 2008; Belokurov et al. 2009; Shu et al. 2017; Sonnenfeld et al. 2018). Similarly, despite the significant boost in classification accuracy offered by CNNs, recent lens searches on multiband imaging using machine learning have also focused on the population of elliptical lens galaxies (e.g. Jacobs et al. 2019; Petrillo et al. 2019; Cañameras et al. 2020). Secondly, automated algorithms based on supervised neural networks reach the best classification performance (Metcalf et al. 2019), but they are strongly dependent on the content of the ground truth data set, and require substantial examples of each morphological class and lens configuration for training. While deep residual networks are able to identify strong lenses with various image separations (e.g. Huang et al. 2020), this poses challenges in developing machine learning pipelines reaching high completeness over broad ranges of lens halo masses ($\approx 10^{11}$ – $10^{15} M_{\odot}$, from isolated galaxies to clusters).

Knabel et al. (2020) compare the citizen science classification of galaxy-scale lenses with automated deep learning and spectroscopic selections over a common footprint covered by the Galaxy and Mass Assembly and Kilo Degree surveys. Interestingly, the independent crowdsourced and machine learning searches result in essentially distinct sets of lens candidates. Despite substantial differences in the parent samples, these findings highlight the complementarity between the two approaches for ground-based searches.

Regarding space-based data, automated lens searches in optical and near-infrared imaging are currently also suffering from limitations. For instance, due to the lack of colour information, the deep learning search conducted in HST data by Pourrahmani et al. (2018) is restricted to the most massive lens ellipticals. The minor overlap with our present sample illustrates again that, even though machine learning reaches higher performance for specific classification tasks (Metcalf et al. 2019), citizen science projects remain key in accessing the broad diversity of strong lenses.

5.4. Future prospects

Given the comparable angular resolution and sampling of *Euclid* and HST images, our results highlight the range of strong lensing studies that will become accessible with the wide *Euclid* survey. Given the large variety of lens configurations targeted in our archival search, and given the in-homogeneous selection process involving images with different depths and taken in different filters, we can not robustly measure the sample completeness. It is nonetheless interesting to note that our overall number of strong lens candidates is comparable to the re-scaled *Euclid* forecasts. Collett (2015) predicted that 170 000 galaxy-scale strong lenses will be discoverable from the final stack of the *Euclid* survey, for lens early-type galaxies and various assumptions on the source population and detectability criteria. This corresponds to ≈ 300 strong lenses discoverable over our 27 deg² footprint, while we found ≈ 240 non-targeted candidates from the ACS and WFC3/UVIS classifications, including a few group-, cluster-scale and more exotic lenses which are not considered by Collett (2015).

This adds further evidence that *Euclid* will be able to find large samples of $>100\,000$ strong lenses, while covering much broader ranges in lens redshifts and extending robust mass measurements to $z > 1$. Strong lens searches in *Euclid* will likely benefit from joining CNN and crowdsourced classifications, for

instance by involving citizens to assemble representative training sets, or to clean the contaminants from CNN selections in order to increase the sample purity.

6. Conclusion

We present a sample of 198 new, high-quality strong lens candidates identified in 18 years of HST archival data. We performed a systematic search for non-targeted strong gravitational lenses in the entire HST archive, by inspecting observations taken with the ACS and WFC3 instruments between 2002 and 2020 with crowdsourcing.

We find 252 strong gravitational lens candidates appearing serendipitously in HST observations, after excluding targeted observations of known lenses. 54 of them have been previously mentioned in other studies, as presented in Table A.2. A total of 198 strong lens candidates were not previously reported in the literature. We categorised them into 45 grade A, 74 grade B, and 79 grade C based on their morphology, the shape of the source image, and the quality and availability of an HST colour image. Our selection purely based on morphological criteria results in strong lenses with various lens and source galaxy types, and various image multiplicities and angular distributions. This shows the potential of citizen science in accessing the broad diversity of strong lenses, and the complementarity with automated classification algorithms.

The sample contains a majority of extended, distorted arcs and rings, which are less ambiguous than compact lensed sources. While 124 (63%) of the new strong lenses are associated with foreground spectroscopically-confirmed or candidate galaxy clusters, most of them have galaxy-scale configurations, with the light deflection dominated by a single member or line-of-sight galaxy. For instance, only three new grade A show a major contribution from the cluster-scale mass component. In addition, while we find a majority of lenses being ellipticals, $\lesssim 10\%$ of the foreground lens galaxies have light profiles consistent with exponential discs, corresponding either to edge-on or to moderately inclined spirals. Finally, a few systems have exotic configurations such as possible double source plane lenses.

In terms of distributions, the newly detected lenses are, on average, 1.3 magnitudes fainter than previous HST searches. The angular separations between multiple images are typically smaller than for lenses found in ground-based data. A quarter of our newly discovered systems have arc radii $\leq 0.82''$, showing the advantage of combining high-resolution of HST imaging with crowdsourcing to select the most compact, galaxy-scale strong lenses for galaxy evolution studies. The redshift distribution of the lens galaxies in our sample is consistent with the lens redshifts from previous ground-based searches.

Since we did not restrict our search to postage stamps of massive elliptical galaxies, as commonly done in strong lens searches, our study constitutes an unbiased search for lenses with the highest resolution currently possible with HST. This overall sample of 252 strong lenses is a useful benchmark for future lens searches in high-resolution images, such as those with *Euclid*, JWST or *Roman*.

This paper shows that crowdsourcing is a robust method to perform visual detection of strong lenses. Indeed, after receiving proper training and knowledge transfer, the volunteers demonstrated their ability to detect classical lenses as well as outliers such as exotic lens configurations. Although inspecting large field of view images might lead to a decrease in completeness, this approach has the advantage of considerably speeding up the detection process compared to inspecting postage stamps, where

a pre-selection of the targets is often necessary. In addition, providing metadata for the images, such as the coordinates and links to ESASky, enabled the volunteers to perform further analysis and identify the objects in the archives. While using colour images for the inspection might have led to a larger number of lenses being identified, multiple bands were only available for a fraction of the Hubble images in the archives. Nevertheless, the volunteers demonstrated that they are able to identify strong lenses in grey-scale images, which is an important lesson for *Euclid*, where only a single optical band is available. It is important to note that, while it is significantly faster for thousands of citizen scientists to inspect the images than for a handful of professional astronomers, it still took one year of volunteer effort to explore more than 45 000 HST observations. Given the scale of *Euclid*, a citizen science approach to explore the entire *Euclid* dataset of $\approx 15\,000\text{ deg}^2$ is not feasible on its own. Combining artificial intelligence methods and crowdsourcing for the detection of strong lenses, for example through iterative training and validation, has thus a strong potential to produce reliable catalogues in shorter timescales and detect outliers such as exotic lenses. Our study also demonstrates the potential for using crowdsourcing to explore the growing JWST archives of images for strong gravitational lenses, as the high-resolution, infrared and multi-wavelength JWST observations will reveal even higher redshift lenses and with smaller Einstein radii.

To conclude, this series of Hubble Asteroid Hunter papers reaffirmed the importance of crowdsourcing in visually detecting complex objects such as strong gravitational lenses and Solar System objects. It also showed the benefits of exploring large archival datasets spanning decades in time to expand the horizons of future research.

Acknowledgements. We acknowledge the tremendous work made by the citizen scientist volunteers on the Hubble Asteroid Hunter project. Their contributions are individually acknowledged on <https://www.zooniverse.org/projects/sandorkruk/hubble-asteroid-hunter/about/results>.

We thank the anonymous referee for their detailed and insightful comments, as they greatly contributed to enhance the quality of our paper. We thank Stella Seitz and Sherry Suyu for insightful discussions on the sample of strong gravitational lenses.

This work has been conducted by EOG as part of the European Space Agency (ESA) student internship. SK and RB gratefully acknowledge support from the ESA Research Fellowship.

This paper is based on observations made with the NASA/ESA *Hubble Space Telescope*, obtained from the data archive at the Space Telescope Science Institute. STScI is operated by the Association of Universities for Research in Astronomy, Inc. under NASA contract NAS 5-26555. Based on observations made with the NASA/ESA *Hubble Space Telescope*, and obtained from the Hubble Legacy Archive, which is a collaboration between the Space Telescope Science Institute (STScI/NASA), the Space Telescope European Coordinating Facility (ST-ECF/ESA) and the Canadian Astronomy Data Centre (CADC/NRC/CSA).

The new strong lens candidates (Table A.1) were found in the following HST programs: 9405, 9414, 9427, 9458, 9476, 9483, 9500, 9722, 9753, 9770, 9822, 9836, 10096, 10134, 10152, 10200, 10207, 10325, 10326, 10334, 10395, 10420, 10491, 10496, 10503, 10504, 10505, 10521, 10523, 10569, 10626, 10635, 10816, 10825, 10861, 10875, 10880, 10881, 10997, 11142, 11588, 11597, 11613, 11697, 11734, 12063, 12064, 12104, 12166, 12195, 12209, 12238, 12253, 12286, 12313, 12319, 12362, 12476, 12477, 12515, 12546, 12549, 12555, 12575, 12591, 12756, 12884, 12898, 12937, 13023, 13024, 13307, 13352, 13364, 13393, 13412, 13442, 13495, 13496, 13514, 13641, 13657, 13695, 13698, 13711, 13750, 13845, 13942, 14096, 14098, 14118, 14165, 14199, 14594, 14662, 14766, 14808, 15063, 15117, 15121, 15183, 15212, 15230, 15275, 15287, 15307, 15320, 15378, 15446, 15495, 15608, 15642, 15644, 15654, 15696, 15843, 16025. We are extremely grateful to the PIs of the HST observations for their positive feedback and responses in including the objects in our catalogue and for the useful conversations.

This publication uses data generated via the Zooniverse.org platform, development of which is funded by generous support, including a Global Impact Award from Google, and by a grant from the Alfred P. Sloan Foundation. Funding for the SDSS and SDSS-II has been provided by the Alfred P. Sloan Foundation, the Participating Institutions, the National Science Foundation, the U.S. Department of Energy, the National Aeronautics and Space Administration, the Japanese Monbukagakusho, the Max Planck Society, and the Higher Education Funding Council for England. The SDSS Web Site is <http://www.sdss.org/>.

The SDSS is managed by the Astrophysical Research Consortium for the Participating Institutions. The Participating Institutions are the American Museum of Natural History, Astrophysical Institute Potsdam, University of Basel, University of Cambridge, Case Western Reserve University, University of Chicago, Drexel University, Fermilab, the Institute for Advanced Study, the Japan Participation Group, Johns Hopkins University, the Joint Institute for Nuclear Astrophysics, the Kavli Institute for Particle Astrophysics and Cosmology, the Korean Scientist Group, the Chinese Academy of Sciences (LAMOST), Los Alamos National Laboratory, the Max-Planck-Institute for Astronomy (MPIA), the Max-Planck-Institute for Astrophysics (MPA), New Mexico State University, Ohio State University, University of Pittsburgh, University of Portsmouth, Princeton University, the United States Naval Observatory and the University of Washington.

This research made use of NASA's Astrophysics Data System Bibliographic Services. This work made extensive use of *Astropy*⁷, a community-developed core Python package for Astronomy (Price-Whelan et al. 2018) and of the Tool for Operations on Catalogues And Tables (TOPCAT⁸; Taylor 2005). This publication used GALFIT (Peng et al. 2002) and SExtractor (Bertin & Arnouts 1996) for the lens fitting and parameter retrieval, as well as the software tool R (R Core Team 2020) and its packages vplot (Adler & Kelly 2020) and Hmisc (Harrell Jr & Harrell Jr 2019) for preparation of the tables and data visualisation. This work also made use of Xmatch (Budavari & Lee 2013) and TOPCAT to perform cross-matching of the lenses with nearby clusters.

References

- Adler, D. & Kelly, S. T. 2020, vplot: violin plot, r package version 0.3.7
- Ahumada, R., Prieto, C. A., Almeida, A., et al. 2020, *ApJS*, 249, 3
- Alard, C. 2006, arXiv e-prints, astro
- Atek, H., Richard, J., Kneib, J.-P., et al. 2014, *ApJ*, 786, 60
- Barnabè, M., Czoske, O., Koopmans, L. V. E., et al. 2009, *MNRAS*, 399, 21
- Belokurov, V., Evans, N. W., Hewett, P. C., et al. 2009, *MNRAS*, 392, 104
- Bertin, E. & Arnouts, S. 1996, *A&AS*, 117, 393
- Bettoni, D., Falomo, R., Scarpa, R., et al. 2019, *ApJ*, 873, L14
- Bhatawdekar, R. & Conselice, C. J. 2021, *ApJ*, 909, 144
- Bhatawdekar, R., Conselice, C. J., Margalef-Bentabol, B., & Duncan, K. 2019, *MNRAS*, 486, 3805
- Bolton, A. S., Brownstein, J. R., Kochanek, C. S., et al. 2012, *ApJ*, 757, 82
- Bolton, A. S., Burles, S., Koopmans, L. V. E., et al. 2008, *ApJ*, 682, 964
- Bom, C. R., Makler, M., Albuquerque, M. P., & Brandt, C. H. 2017, *A&A*, 597, A135
- Brownstein, J. R., Bolton, A. S., Schlegel, D. J., et al. 2012, *ApJ*, 744, 41
- Budavari, T. & Lee, M. A. 2013, Xmatch: GPU Enhanced Astronomic Catalog Cross-Matching, Astrophysics Source Code Library, record ascl:1303.021
- Cañameras, R., Nesvadba, N., Kneissl, R., et al. 2017, *A&A*, 604, A117
- Cañameras, R., Schuldt, S., Suyu, S. H., et al. 2020, *A&A*, 644, A163
- Cabanac, R. A., Alard, C., Dantel-Fort, M., et al. 2007, *A&A*, 461, 813
- Caminha, G. B., Rosati, P., Grillo, C., et al. 2019, *A&A*, 632, A36
- Cappellari, M., Romanowsky, A. J., Brodie, J. P., et al. 2015, *ApJ*, 804, L21
- Clowe, D., Markevitch, M., Bradač, M., et al. 2012, *The Astrophysical Journal*, 758, 128
- Collett, T. E. 2015, *ApJ*, 811, 20
- Collett, T. E., Auger, M. W., Belokurov, V., Marshall, P. J., & Hall, A. C. 2012, *MNRAS*, 424, 2864
- Courbin, F., Bonvin, V., Buckley-Geer, E., et al. 2018, *A&A*, 609, A71
- Derkenne, C., McDermid, R. M., Poci, A., et al. 2021, *MNRAS*, 506, 3691
- Desprez, G., Richard, J., Jauzac, M., et al. 2018, *MNRAS*, 479, 2630
- Dessauges-Zavadsky, M., Zamojski, M., Schaerer, D., et al. 2015, *A&A*, 577, A50
- Diego, J. M., Broadhurst, T., Benitez, N., Lim, J., & Lam, D. 2015, *MNRAS*, 449, 588
- Dieleman, S., Willett, K. W., & Dambre, J. 2015, *MNRAS*, 450, 1441
- D'Isanto, A. & Polsterer, K. L. 2018, *A&A*, 609, A111
- Ebeling, H., Atek, H., Edge, A. C., et al. 2019, Beyond MACS: A Snapshot Survey of the Most Massive Clusters of Galaxies at $z=0.5-1$, HST Proposal
- Ebeling, H. & Kalita, B. S. 2019, *ApJ*, 882, 127
- Ebeling, H., Ma, C.-J., & Barrett, E. 2014, *ApJS*, 211, 21
- Ebeling, H., Stockmann, M., Richard, J., et al. 2018, *ApJ*, 852, L7
- Fassnacht, C. D., Moustakas, L. A., Casertano, S., et al. 2004, *ApJ*, 600, L155
- Faure, C., Kneib, J.-P., Covone, G., et al. 2008, *ApJS*, 176, 19
- Fort, B., Le Fevre, O., Hammer, F., & Cailloux, M. 1992, *ApJ*, 399, L125
- Gavazzi, R., Marshall, P. J., Treu, T., & Sonnenfeld, A. 2014, *ApJ*, 785, 144
- Gavazzi, R., Treu, T., Koopmans, L. V. E., et al. 2008, *ApJ*, 677, 1046
- Giordano, F., Racero, E., Norman, H., et al. 2018, *Astronomy and Computing*, 24, 97
- Gonzaga, S., Hack, W., Fruchter, A., & Mack, J. 2012, *The DrizzlePac Handbook* (Baltimore, STScI)
- Grillo, C., Lombardi, M., Rosati, P., et al. 2008, *A&A*, 486, 45
- Grozin, N. A., Kocevski, D. D., Faber, S. M., et al. 2011, *ApJS*, 197, 35
- Guzzo, L., Schuecker, P., Böhringer, H., et al. 2009, *A&A*, 499, 357
- Harrell Jr, F. E. & Harrell Jr, M. F. E. 2019, CRAN2018, 2019, 235
- Holwerda, B. W., Baldry, I. K., Alpaslan, M., et al. 2015, *MNRAS*, 449, 4277
- Horesh, A., Maoz, D., Ebeling, H., Seidel, G., & Bartelmann, M. 2010, *MNRAS*, 406, 1318
- Huang, X., Storfer, C., Ravi, V., et al. 2020, *ApJ*, 894, 78
- Huertas-Company, M., Gravet, R., Cabrera-Vives, G., et al. 2015, *ApJS*, 221, 8
- Jackson, N. 2008, *MNRAS*, 389, 1311
- Jacobs, C., Collett, T., Glazebrook, K., et al. 2019, *ApJS*, 243, 17
- Jarosik, N., Bennett, C. L., Dunkley, J., et al. 2011, *ApJS*, 192, 14
- Jauzac, M., Richard, J., Jullo, E., et al. 2015, *MNRAS*, 452, 1437
- Kelly, P. L., Rodney, S. A., Treu, T., et al. 2015, *Science*, 347, 1123
- Kikuchi, S., Ouchi, M., Ono, Y., et al. 2020, *ApJ*, 893, 60
- Knabel, S., Steele, R. L., Holwerda, B. W., et al. 2020, *AJ*, 160, 223
- Koekemoer, A. M., Aussel, H., Calzetti, D., et al. 2007, *ApJS*, 172, 196
- Koester, B. P., Gladders, M. D., Hennawi, J. F., et al. 2010, *ApJ*, 723, L73
- Koopmans, L. V. E., Treu, T., Bolton, A. S., Burles, S., & Moustakas, L. A. 2006, *ApJ*, 649, 599
- Krist, J. 1995, in *Astronomical Society of the Pacific Conference Series*, Vol. 77, *Astronomical Data Analysis Software and Systems IV*, ed. R. A. Shaw, H. E. Payne, & J. J. E. Hayes, 349
- Kruk, S., García Martín, P., Popescu, M., et al. 2022, arXiv e-prints, arXiv:2202.00246
- Küng, R., Saha, P., More, A., et al. 2015, *Monthly Notices of the Royal Astronomical Society*, 447, 2170
- Lagattuta, D. J., Fassnacht, C. D., Auger, M. W., et al. 2010, *ApJ*, 716, 1579
- Li, R., Shu, Y., & Wang, J. 2018, *MNRAS*, 480, 431
- Lintott, C. J., Schawinski, K., Slosar, A., et al. 2008, *MNRAS*, 389, 1179
- Livermore, R. C., Finkelstein, S. L., & Lotz, J. M. 2017, *ApJ*, 835, 113
- Marshall, P. J., Hogg, D. W., Moustakas, L. A., et al. 2009, *ApJ*, 694, 924
- Marshall, P. J., Treu, T., Melbourne, J., et al. 2007, *ApJ*, 671, 1196
- Marshall, P. J., Verma, A., More, A., et al. 2016, *MNRAS*, 455, 1171
- Metcalf, R. B., Meneghetti, M., Avestruz, C., et al. 2019, *A&A*, 625, A119
- Millon, M., Galan, A., Courbin, F., et al. 2020, *A&A*, 639, A101
- More, A., Cabanac, R., More, S., et al. 2012, *ApJ*, 749, 38
- More, A., Jahnke, K., More, S., et al. 2011, *ApJ*, 734, 69
- More, A., Verma, A., Marshall, P. J., et al. 2016, *MNRAS*, 455, 1191
- Morishita, T., Abramson, L. E., Treu, T., et al. 2017, *The Astrophysical Journal*, 835, 254
- Moustakas, L. A., Marshall, P., Newman, J. A., et al. 2007, *ApJ*, 660, L31
- Oguri, M. & Marshall, P. J. 2010, *MNRAS*, 405, 2579
- Oldham, L. J. & Auger, M. W. 2018, *MNRAS*, 476, 133
- Pawase, R. S., Courbin, F., Faure, C., Kokotanekova, R., & Meylan, G. 2014, *MNRAS*, 439, 3392
- Peng, C. Y., Ho, L. C., Impey, C. D., & Rix, H.-W. 2002, *AJ*, 124, 266
- Petrillo, C. E., Tortora, C., Vernardos, G., et al. 2019, *MNRAS*, 484, 3879
- Pourrahmani, M., Nayyeri, H., & Cooray, A. 2018, *ApJ*, 856, 68
- Price-Whelan, A. M., Sipőcz, B., Günther, H., et al. 2018, *The Astronomical Journal*, 156, 123
- R Core Team. 2020, R: A Language and Environment for Statistical Computing, R Foundation for Statistical Computing, Vienna, Austria
- Ragozzine, B., Clowe, D., Markevitch, M., Gonzalez, A. H., & Bradač, M. 2012, *ApJ*, 744, 94
- Ratnatunga, K. U., Ostrander, E. J., Griffiths, R. E., & Im, M. 1995, *ApJ*, 453, L5
- Repp, A. & Ebeling, H. 2018, *MNRAS*, 479, 844
- Richard, J., Patricio, V., Martinez, J., et al. 2015, *MNRAS*, 446, L16
- Richard, J., Smith, G. P., Kneib, J.-P., et al. 2010, *MNRAS*, 404, 325
- Ritondale, E., Vegetti, S., Despali, G., et al. 2019, *MNRAS*, 485, 2179
- Rojas, K., Savary, E., Clément, B., et al. 2021, arXiv e-prints, arXiv:2109.00014
- Rykoff, E. S., Rozo, E., Busha, M. T., et al. 2014, *ApJ*, 785, 104
- Rykoff, E. S., Rozo, E., Busha, M. T., et al. 2016, *VizieR Online Data Catalog*, J/ApJ/785/104
- Samui, S. & Samui Pal, S. 2017, *New A*, 51, 169

⁷ <http://www.astropy.org/>

⁸ <http://www.star.bris.ac.uk/~mbt/>

- Schaefer, C., Geiger, M., Kuntzer, T., & Kneib, J. P. 2018, *A&A*, 611, A2
 Schirmer, M., Suyu, S., Schrabback, T., et al. 2010, *A&A*, 514, A60
 Schuldt, S., Suyu, S. H., Cañameras, R., et al. 2021, *A&A*, 651, A55
 Scoville, N., Aussel, H., Brusa, M., et al. 2007, *ApJS*, 172, 1
 Sereno, M. & Paraficz, D. 2014, *MNRAS*, 437, 600
 Sersic, J. L. 1968, *Atlas de Galaxias Australes*
 Sharon, K., Bayliss, M. B., Dahle, H., et al. 2020, *ApJS*, 247, 12
 Shu, Y., Bolton, A. S., Kochanek, C. S., et al. 2016, *ApJ*, 824, 86
 Shu, Y., Brownstein, J. R., Bolton, A. S., et al. 2017, *ApJ*, 851, 48
 Smail, I., Swinbank, A. M., Richard, J., et al. 2007, *ApJ*, 654, L33
 Sonnenfeld, A., Chan, J. H. H., Shu, Y., et al. 2018, *PASJ*, 70, S29
 Sonnenfeld, A., Treu, T., Gavazzi, R., et al. 2013, *ApJ*, 777, 98
 Sonnenfeld, A., Treu, T., Marshall, P. J., et al. 2015, *ApJ*, 800, 94
 Sonnenfeld, A., Verma, A., More, A., et al. 2020, *A&A*, 642, A148
 Stark, D. P., Auger, M., Belokurov, V., et al. 2013, *Monthly Notices of the Royal Astronomical Society*, 436, 1040
 Suyu, S. H., Marshall, P. J., Auger, M. W., et al. 2010, *ApJ*, 711, 201
 Suyu, S. H., Treu, T., Hilbert, S., et al. 2014, *ApJ*, 788, L35
 Swinbank, A. M., Dye, S., Nightingale, J. W., et al. 2015, *ApJ*, 806, L17
 Talbot, M. S., Brownstein, J. R., Dawson, K. S., Kneib, J.-P., & Bautista, J. 2021, *MNRAS*, 502, 4617
 Tanaka, M., Wong, K. C., More, A., et al. 2016, *ApJ*, 826, L19
 Taylor, M. B. 2005, in *Astronomical Society of the Pacific Conference Series*, Vol. 347, *Astronomical Data Analysis Software and Systems XIV*, ed. P. Shopbell, M. Britton, & R. Ebert, 29
 Treu, T., Dutton, A. A., Auger, M. W., et al. 2011, *MNRAS*, 417, 1601
 Treu, T. & Koopmans, L. V. E. 2004, *ApJ*, 611, 739
 Tu, H., Gavazzi, R., Limousin, M., et al. 2009, *A&A*, 501, 475
 Vanzella, E., Caminha, G. B., Rosati, P., et al. 2021, *A&A*, 646, A57
 Vegetti, S. & Koopmans, L. V. E. 2009, *MNRAS*, 392, 945
 Walmsley, M., Lintott, C., Géron, T., et al. 2022, *MNRAS*, 509, 3966
 Walmsley, M., Smith, L., Lintott, C., et al. 2020, *MNRAS*, 491, 1554
 Walsh, D., Carswell, R. F., & Weymann, R. J. 1979, *Nature*, 279, 381
 Wang, Y., Vogelsberger, M., Xu, D., et al. 2019, *MNRAS*, 490, 5722
 Welch, B., Coe, D., Diego, J. M., et al. 2022, *Nature*, 603, 815
 Wong, K. C., Suyu, S. H., Chen, G. C. F., et al. 2020, *MNRAS*, 498, 1420
 Zitrin, A., Fabris, A., Merten, J., et al. 2015, *The Astrophysical Journal*, 801, 44
 Zou, H., Gao, J., Xu, X., et al. 2021, *ApJS*, 253, 56

Appendix A: List of strong lens candidates

Table A.1. Newly discovered lenses.

IAU Name	ID	RA	Dec	r_{arc} (")	instru.	filter	mag	r_e (")	q	PA	class	clust.	z
A grade Lenses													
HAH J001538.4 – 390435.0	1	3.91007	39.07643	0.79	UVIS	f475w	25.4	0.06	0.93	–81.9	Arc		
HAH J002348.6 – 244149.6	2	5.95275	–24.69702	1.07	ACS	f814w	20.1	1.45	0.56	89.1	Quad	DClust1	
HAH J002753.2 – 753730.0	3	6.97150	–75.62500	1.71	ACS	f606w	19.6	1.10	0.93	–112.6	Ring	DClust2	
HAH J004924.3 – 205729.8	4	12.35113	–20.95829	0.78	ACS	f606w	20.3	0.80	0.77	–19.7	Arc	DClust3	
HAH J005403.4 – 394712.1	5	13.15445	39.78661	2.05	ACS	f814w	20.2	0.85	0.81	155.8	Arc		0.73 P
HAH J015949.3 – 084906.0	6	29.95549	–8.81828	1.17	ACS	f606w	21.1	0.35	0.92	128.6	Arc	DClust4	0.39 P
HAH J021706.2 – 051318.0	7	34.27592	–5.22168	1.14	ACS	f814w	21.7	0.54	0.68	–9.8	Arc		0.59 P
HAH J024329.8 – 593102.7	8	40.87441	–59.51759	0.63	UVIS	f200lp	23.1	0.35	0.81	95.4	Arc	DClust5	
HAH J024533.6 – 530203.5	9	41.39015	–53.03433	0.73	ACS	f814w	20.1	0.39	0.88	–24.2	Ring	DClust6	
HAH J024932.8 + 334635.5	10	42.38714	33.77651	0.55	ACS	f775w	25.1	0.32	0.39	89.7	Arc		
HAH J025241.6 – 150025.5	11	43.17305	–15.00712	3.23	ACS	f814w	21.3	0.36	0.90	–111.1	Arc	DClust7	
HAH J025659.9 – 163059.5	12	44.24984	–16.51655	1.48	ACS	f606w	18.8	2.08	0.71	–164.4	Arc	DClust8	0.31 P
HAH J033603.9 – 451223.1	13	54.01630	–45.20642	0.63	ACS	f814w	22.6	0.31	0.79	–176.5	Ring		
HAH J034445.2 – 642133.8	14	56.18856	–64.35941	1.42	ACS	f606w	24.2	0.10	1.00	153.0	Arc	DClust9	
HAH J042044.0 – 403607.2	15	65.18326	–40.60200	0.42	UVIS	f814w	22.7	0.48	0.84	152.3	Ring		
HAH J054707.0 – 390516.3	16	86.77923	–39.08786	0.74	ACS	f814w	19.7	0.40	0.80	139.2	Ring	DClust10	
HAH J061345.7 – 562750.4	17	93.44050	–56.46400	1.2	ACS	f606w	18.9	1.08	0.42	68.7	Arc	DClust11	
HAH J072221.9 + 072326.7	18	110.59159	7.39076	0.59	ACS	f814w	20.3	0.74	0.91	–99.5	Arc	DClust12	
HAH J081334.8 + 254518.3	19	123.99489	25.75509	1.6	IR	f140w	19.1	1.04	0.83	52.6	Arc		
HAH J083420.3 + 452506.9	20	128.58462	45.41860	1.04	ACS	f814w	21.2	0.65	0.61	–107.9	Arc	DClust13	0.65 S
HAH J084833.4 + 444431.9	21	132.13930	44.74220	1.2	ACS	f814w	22.5	0.27	0.81	120.9	Arc		0.19 P
				1.2	ACS	f814w	24.2	0.22	0.13	–174.1	Arc		0.19 P
				1.2	ACS	f814w	23.6	0.20	0.46	–158.5	Arc		0.19 P
HAH J093325.2 + 284348.6	22	143.35520	28.73018	3.27	ACS	f606w	20.6	0.10	0.77	–130.3	Arc		0.4 P
				3.27	ACS	f606w	19.7	1.38	0.84	–103.8	Arc		0.4 P
HAH J100141.8 + 021424.2	23	150.42410	2.24010	1.46	ACS	f814w	23.7	0.26	0.80	–104.2	Ring		0.34 P
HAH J100251.8 + 691959.3	24	150.71567	69.33316	0.7	ACS	f606w	22.0	1.21	0.22	133.9	Double		0.56 P
HAH J102914.8 + 262207.0	25	157.31170	26.36860	0.64	ACS	f475w	23.6	0.36	0.69	108.2	Arc	DClust14	0.57 P
HAH J105722.7 + 580046.5	26	164.34460	58.01290	0.46	ACS	f814w	22.7	0.32	0.75	–105.9	Arc	DClust15	0.54 P
HAH J111337.4 + 221249.2	27	168.40564	22.21368	2.11	UVIS	f350lp	18.8	1.94	0.74	–135.1	Arc	DClust16	0.41 S
HAH J113158.4 – 195451.5	28	172.99340	–19.91430	1.66	ACS	f814w	18.8	1.25	0.65	114.5	Arc		
HAH J114938.4 + 222107.7	29	177.41020	22.35200	0.8	ACS	f814w	20.8	0.38	0.66	58.8	Arc	DClust17	0.42 P
HAH J121653.9 – 121104.2	30	184.22457	–12.18464	1.12	ACS	f814w	19.2	0.54	0.97	–57.9	Ring		
HAH J125709.5 + 282239.7	31	194.28970	28.37770	0.88	ACS	f475w	26.4	1.48	0.05	140.0	Arc		0.78 P
				0.88	ACS	f475w	24.6	0.17	0.55	–93.9	Arc		0.78 P
HAH J130124.0 – 113114.6	32	195.34996	–11.52072	0.91	ACS	f814w	19.1	1.13	0.67	–29.2	Ring		
HAH J131953.6 + 700420.8	33	199.97339	70.07245	1.16	ACS	f606w	20.0	0.46	0.85	–157.0	Ring	DClust18	
HAH J132824.5 – 313204.6	34	202.10207	–31.53468	1.4	UVIS	f475w	22.0	0.94	0.69	179.8	Arc		
HAH J133525.9 + 405952.4	35	203.85800	40.99790	0.95	ACS	f814w	18.9	1.49	0.74	102.6	Arc	DClust19	0.29 P
HAH J135955.7 + 143820.4	36	209.98235	14.63882	0.56	UVIS	f390w	22.9	0.55	0.94	44.7	Arc		
HAH J141139.2 + 565200.9	37	212.91351	56.86694	0.51	UVIS	f475x	21.2	0.74	0.45	92.6	Ring	DClust20	
HAH J141900.1 + 524249.0	38	214.71505	52.71360	1.12	ACS	f814w	20.9	0.44	0.94	–136.8	Arc		0.46 P
HAH J143811.5 + 464007.6	39	219.54794	46.66877	0.57	ACS	f435w	22.1	0.46	0.46	–118.5	Ring		
HAH J163124.5 + 124304.3	40	247.85224	12.71771	2.31	UVIS	f814w	22.5	0.52	0.92	–45.1	Arc		0.64 S
HAH J163417.6 + 703107.0	41	248.57350	70.51860	1.13	IR	f140w	19.1	0.46	0.93	138.3	Arc		
HAH J171314.9 + 602207.7	42	258.31200	60.36890	0.94	ACS	f814w	21.2	0.27	0.62	–17.9	Ring		0.26 P
				0.94	ACS	f814w	24.6	1.95	0.00	–28.7	Ring		0.26 P
HAH J214817.6 – 484350.5	43	327.07301	–48.73045	1.12	UVIS	f200lp	23.1	0.39	0.89	98.0	Arc	DClust21	
HAH J215849.5 – 223159.7	44	329.70656	–22.53325	3.27	ACS	f775w	19.2	2.38	0.68	–23.8	Arc		
HAH J234106.5 – 000007.5	45	355.27743	–0.00210	2.31	UVIS	f390w	19.9	1.43	0.92	–50.2	Arc	DClust22	0.19 S
B grade Lenses													
HAH J001419.9 – 302600.7	46	3.58309	–30.43355	1.3	ACS	f814w	18.6	0.93	0.67	177.1	Arc	DClust23	0.29 ★
HAH J002706.3 + 170313.5	47	6.77622	17.05375	0.8	ACS	f814w	21.5	0.72	0.67	–174.9	Arc	DClust24	
HAH J003350.8 – 074959.9	48	8.46170	–7.83330	0.88	ACS	f814w	22.1	0.45	0.65	–95.4	Arc	DClust25	0.16 P
HAH J004426.2 – 403941.4	49	11.10937	–40.66150	0.55	ACS	f606w	23.9	0.44	0.71	–120.6	Ring	DClust26	
HAH J004859.0 + 401706.7	50	12.24571	40.28517	1.05	ACS	f606w	24.6	0.30	0.29	69.4	Arc		
HAH J005141.6 + 272001.5	51	12.92343	27.33376	1.3	IR	f110w	17.6	0.81	0.97	–1.4	Arc	DClust27	0.36 P
HAH J011138.3 – 454015.1	52	17.90972	–45.67088	0.93	IR	f105w	19.4	0.29	0.82	146.2	Arc	DClust28	
HAH J013723.7 – 082852.2	53	24.34861	–8.48115	1.87	ACS	f606w	20.1	0.43	0.88	–178.1	Arc	DClust29	0.52 P
HAH J015256.3 – 135416.3	54	28.23476	–13.90454	0.59	ACS	f814w	21.9	0.55	0.73	–86.4	Arc		
HAH J022056.4 – 033332.1	55	35.23505	–3.55899	1.46	ACS	f850lp	21.5	0.33	0.56	–130.1	Arc		
HAH J023951.1 – 013205.9	56	39.96294	–1.53500	1.1	ACS	f814w	19.8	0.45	0.68	0.2	Arc	DClust30	0.48 P
HAH J024535.7 – 530125.5	57	41.39911	–53.02377	0.86	ACS	f814w	20.0	0.61	0.48	–11.2	Arc	DClust31	
HAH J025735.5 – 220928.5	58	44.39802	–22.15791	0.84	ACS	f814w	18.8	1.84	0.74	–161.8	Arc	DClust32	
HAH J025740.9 – 221027.3	59	44.42063	–22.17426	0.85	ACS	f814w	20.0	0.29	0.59	168.8	Arc	DClust33	
HAH J032030.9 + 003242.8	60	50.12858	0.54522	2.91	ACS	f775w	19.4	0.69	0.53	–102.5	Arc	DClust34	0.39 S
HAH J033305.9 – 274744.8	61	53.27467	–27.79577	1.3	ACS	f606w	21.1	0.37	0.74	–174.9	Arc		0.35 P★
HAH J033530.7 – 540734.7	62	53.87735	–54.12630	3.23	ACS	f814w	20.2	1.17	0.34	–4.0	Arc	DClust35	
				3.23	ACS	f814w	20.0	15.49	0.52	–0.1	Arc		
HAH J033645.9 – 535536.7	63	54.18759	–53.92647	1.21	UVIS	f814w	20.4	0.33	0.77	–149.5	Arc	DClust36	
HAH J035851.7 – 295418.7	64	59.71560	–29.90520	1	ACS	f814w	20.1	0.50	0.76	–28.2	Arc	DClust37	0.42 ★
HAH J041631.5 – 240512.5	65	64.13140	–24.08680	1.23	ACS	f814w	21.1	1.06	0.34	–116.5	Double	DClust38	
HAH J044208.3 – 281503.7	66	70.53440	–28.25102	4.4	ACS	f814w	19.9	1.16	0.58	–103.0	Arc	DClust39	
				4.4	ACS	f814w	19.5	1.62	0.66	–46.3	Arc		
HAH J045430.7 – 030133.2	67	73.62796	–3.02590	1.47	ACS	f814w	20.3	0.66	0.77	–97.0	Arc	DClust40	

Table A.1. *continued.*

IAU Name	ID	RA	Dec	$r_{\text{arc}} (")$	instru.	filter	mag	$r_c (")$	q	PA	class	clust.	z
HAH J045441.7 – 030319.9	68	73.67378	-3.05553	1.18	ACS	f814w	20.1	0.51	0.76	-82.1	Arc	DClust41	0.61 P
HAH J051850.3 – 431442.0	69	79.70954	-43.24500	1.56	ACS	f814w	21.4	1.10	0.80	99.1	Arc	DClust42	
HAH J055326.6 – 334254.0	70	88.36070	-33.71500	2.65	ACS	f814w	20.0	0.36	0.77	-18.5	Arc	DClust43	
HAH J065821.5 – 555711.5	71	104.58970	-55.95316	1.88	ACS	f606w	19.9	0.87	0.43	-88.6	Arc		
HAH J072218.2 + 072314.8	72	110.57599	7.38745	0.6	ACS	f814w	21.4	0.44	0.60	146.3	Arc	DClust44	
HAH J072333.8 – 732550.9	73	110.89080	-73.43080	0.97	ACS	f814w	21.3	0.42	0.31	139.8	Arc	DClust45	
HAH J074421.4 + 375400.0	74	116.08890	37.89990	1.27	UVIS	f606w	24.3	0.40	0.28	-159.4	Arc		
HAH J074531.3 + 195111.7	75	116.38083	19.85327	0.73	UVIS	f606w	22.4	0.45	0.79	112.4	Double		0.44 P
HAH J083410.0 + 491332.2	76	128.54159	49.22560	0.85	ACS	f606w	23.0	0.83	0.46	-8.7	Arc		
HAH J084712.7 + 344910.9	77	131.80310	34.81970	0.69	ACS	f814w	22.9	0.13	0.84	26.1	Arc	DClust46	
HAH J091503.8 + 581147.7	78	138.76580	58.19660	0.85	UVIS	f350lp	22.8	0.50	0.89	134.8	Ring		
HAH J094949.9 + 170614.4	79	147.45790	17.10399	2.3	ACS	f814w	19.8	0.57	0.40	30.4	Arc	DClust47	0.39 P
HAH J095549.0 – 100034.8	80	148.95441	-10.00973	1.16	ACS	f606w	24.5	0.47	0.34	36.0	Arc		
HAH J095633.6 – 100913.3	81	149.13990	-10.15370	1.31	ACS	f606w	17.6	2.00	0.86	19.2	Arc		
HAH J095712.5 + 690709.1	82	149.30206	69.11924	3.79	ACS	f814w	19.7	0.96	0.81	145.4	Arc		0.52 P
				3.79	ACS	f814w	20.4	1.01	0.70	-139.8	Arc		0.52 P
HAH J095803.9 + 653409.1	83	149.51620	65.56920	1.44	ACS	f814w	21.0	1.66	0.77	4.4	Arc	DClust48	
HAH J100030.1 + 023716.7	84	150.12550	2.62130	0.84	ACS	f814w	25.6	0.03	0.41	39.6	Arc	DClust49	0.52 P
				0.84	ACS	f814w	24.8	0.36	0.27	-103.8	Arc		0.52 P
				0.84	ACS	f814w	24.5	2.60	0.42	-93.1	Arc		0.52 P
HAH J100124.2 + 555407.2	85	150.35080	55.90200	1.45	ACS	f814w	21.2	0.13	0.62	-165.7	Arc	DClust50	0.36 S
				1.45	ACS	f814w	20.8	0.70	0.35	-169.3	Arc		0.36 S
HAH J103937.6 – 001421.5	86	159.92930	-0.26555	0.51	ACS	f814w	21.4	1.10	0.90	-24.6	Arc		0.23 P
HAH J104001.6 + 474558.0	87	160.00670	47.76612	0.60	ACS	f435w	22.8	0.53	0.50	60.0	Arc		0.35 P
HAH J104132.0 + 000125.0	88	160.38332	-0.02360	0.99	ACS	f606w	23.7	0.62	0.88	45.9	Ring	DClust51	0.67 P
HAH J105726.9 + 575944.0	89	164.36207	57.99555	1.47	ACS	f814w	22.1	0.43	0.43	-157.7	Arc	DClust52	0.24 P
HAH J111507.3 + 531955.8	90	168.78051	53.33217	1.12	ACS	f606w	21.2	0.33	0.62	-136.6	Arc	DClust53	0.44 P
HAH J111822.1 + 033802.1	91	169.59242	3.63393	1.33	IR	f110w	17.4	1.10	0.60	-44.4	Ring	DClust54	0.42 S
HAH J115940.8 + 011410.7	92	179.92011	1.23632	2.5	ACS	f606w	23.3	2.94	0.56	-102.7	Arc		0.44 S
HAH J122944.7 + 112238.3	93	187.43610	11.37730	1.3	ACS	f814w	20.2	0.26	0.80	84.3	Arc	DClust55	0.41 P
HAH J123430.7 + 080444.4	94	188.62785	8.07903	2.1	ACS	f814w	20.3	1.22	0.85	130.0	Arc		0.5 S
HAH J123618.8 + 260905.0	95	189.07830	26.15140	1.54	ACS	f814w	21.3	0.66	0.68	-50.9	Arc	DClust56	
HAH J124756.2 + 134103.3	96	191.98435	13.68426	1.65	ACS	f814w	22.0	1.34	0.86	105.2	Arc		
HAH J125907.8 – 014439.0	97	194.78235	-1.74418	0.33	ACS	f814w	22.2	0.68	0.26	-164.8	Double	DClust57	
HAH J130034.4 + 280022.4	98	195.14321	28.00622	0.7	ACS	f814w	20.7	0.20	0.61	174.3	Arc		0.49 P
HAH J130152.7 + 275147.7	99	195.46939	27.86325	2.17	ACS	f475x	20.2	1.15	0.84	157.9	Arc	DClust58	0.27 S
HAH J132217.5 + 464630.4	100	200.57300	46.77510	3.19	ACS	f814w	18.4	1.49	0.66	-60.9	Arc	DClust59	0.37 S
HAH J132331.9 + 302155.8	101	200.88300	30.36550	2.5	ACS	f814w	21.1	0.36	0.87	64.7	Arc	DClust60	0.46 S
				2.5	ACS	f814w	19.3	0.82	0.73	70.1	Arc		0.46 S
HAH J132529.1 – 474019.2	102	201.37147	-47.67202	0.71	UVIS	f814w	21.4	0.40	0.95	-65.8	Ring		
HAH J133240.6 + 503315.5	103	203.16900	50.55430	3.3	ACS	f814w	19.8	0.46	0.93	-142.5	Arc	DClust61	0.33 P
HAH J133252.7 + 503026.9	104	203.21991	50.50747	1.45	ACS	f814w	18.7	2.39	0.80	-150.4	Arc	DClust62	0.29 P
HAH J135953.3 + 623118.4	105	209.97199	62.52180	2.56	ACS	f814w	19.0	1.03	0.58	-126.6	Arc	DClust63	0.35 P
HAH J143236.3 + 344030.4	106	218.15140	34.67510	1.63	ACS	f814w	20.1	0.77	0.73	30.6	Arc	DClust64	0.57 P
HAH J145832.7 – 002349.9	107	224.63646	-0.39719	0.71	UVIS	f475x	23.1	0.40	1.00	-34.0	Arc	DClust65	0.6 S
HAH J151841.7 + 084549.2	108	229.67379	8.76369	2.01	ACS	f814w	19.7	0.58	0.95	140.9	Arc	DClust66	0.49 P
HAH J161311.2 + 565004.1	109	243.29650	56.83446	0.95	IR	f140w	19.8	0.75	0.79	100.9	Arc	DClust67	0.4 P
HAH J161420.9 + 323306.1	110	243.58700	32.55170	1.17	ACS	f814w	21.4	0.41	0.46	4.5	Arc		
HAH J162122.2 + 381006.5	111	245.34262	38.16847	0.91	ACS	f814w	21.7	0.50	1.00	-70.2	Arc	DClust68	0.2 S
HAH J173146.2 + 225237.6	112	262.94232	22.87712	1.14	ACS	f814w	18.8	0.84	0.75	49.7	Arc	DClust69	0.44 P
HAH J174109.0 + 690236.1	113	265.28755	69.04336	4.45	ACS	f814w	21.5	0.31	0.87	-61.1	Arc		
HAH J180652.4 + 292945.3	114	271.71867	29.49593	0.87	ACS	f606w	21.4	0.23	0.83	8.8	Arc	DClust70	
HAH J191700.9 – 333207.0	115	289.25409	-33.53530	1.29	ACS	f814w	19.1	1.14	0.75	-71.3	Arc	DClust71	
HAH J191709.5 – 333127.0	116	289.28972	-33.52418	0.67	ACS	f814w	22.5	0.17	0.56	10.2	Arc	DClust72	
HAH J204548.7 – 243833.2	117	311.45298	-24.64258	1.52	ACS	f814w	19.6	0.77	0.94	-167.5	Arc		
HAH J224324.6 – 093617.3	118	340.85260	-9.60480	2.06	ACS	f606w	21.1	1.22	0.37	120.6	Arc	DClust73	0.44 P
HAH J233220.8 – 535909.8	119	353.08657	-53.98605	1.26	IR	f140w	17.2	0.72	0.85	-7.2	Arc	DClust74	0.4 ★
C grade Lenses													
HAH J000146.0 – 544026.2	120	0.44161	-54.67395	1.15	ACS	f606w	20.9	0.54	0.92	-118.0	Arc	DClust75	
HAH J002357.7 – 244154.3	121	5.99142	-24.69858	0.88	ACS	f606w	23.2	0.85	0.72	-146.0	Arc	DClust76	
HAH J002616.0 – 110548.2	122	6.56680	-11.09673	2.9	ACS	f814w	20.9	0.90	0.67	87.6	Arc		0.35 P
HAH J003501.7 + 023358.6	123	8.75690	2.56628	2.25	ACS	f814w	18.9	0.78	0.7	-144.6	Arc	DClust77	0.38 P
HAH J004802.0 + 402624.1	124	12.00867	40.44004	1.4	ACS	f814w	20.0	0.67	0.36	133.2	Arc		0.54 P
HAH J013726.6 – 082747.9	125	24.36080	-8.46330	2.5	ACS	f814w	18.4	1.60	0.75	-134.7	Double	DClust78	0.29 P
HAH J014236.3 + 144114.3	126	25.65113	14.68730	1.5	ACS	f775w	19.3	1.18	0.96	174.8	Arc		0.5 S
HAH J015246.7 + 360750.5	127	28.19450	36.13070	0.85	ACS	f435w	22.8	1.23	0.75	-89.5	Ring x 2	DClust79	
HAH J015317.2 – 135220.6	128	28.32207	-13.87241	0.65	ACS	f814w	21.4	0.40	0.69	-137.8	Arc	DClust80	
HAH J022141.7 – 032038.9	129	35.42410	-3.34414	1.25	ACS	f850lp	20.4	0.79	0.67	-101.9	Arc		0.46 P
HAH J022253.9 + 422616.4	130	35.72461	42.43789	2.04	ACS	f814w	20.6	0.71	0.66	57.5	Arc		
HAH J023726.4 – 262957.6	131	39.35982	-26.49932	2.76	ACS	f606w	19.3	0.70	0.76	-165.5	Arc	DClust81	
HAH J024336.7 – 483319.4	132	40.90317	-48.55540	1.33	UVIS	f200lp	22.1	0.45	0.75	-98.4	Ring	DClust82	
HAH J030901.7 + 264522.2	133	47.25701	26.75616	1.25	ACS	f814w	18.3	2.26	0.98	-136.6	Arc	DClust83	
HAH J040411.1 – 554433.8	134	61.04657	-55.74273	1.64	ACS	f606w	17.6	1.40	0.64	-158.2	Arc		
HAH J041308.3 – 655338.7	135	63.28420	-65.89428	0.51	ACS	f606w	24.7	0.28	0.82	-156.5	Ring		
HAH J042905.4 – 101206.7	136	67.27276	-10.20188	1.84	IR	f140w	17.8	0.73	0.88	-166.1	Arc	DClust84	
HAH J043916.2 – 460115.2	137	69.81779	-46.02089	0.97	ACS	f606w	21.8	0.17	0.91	175.9	Arc	DClust85	
HAH J044632.8 – 591132.0	138	71.63668	-59.19223	1.5	ACS	f814w	19.9	1.03	0.78	120.5	Arc		
HAH J045159.3 + 000645.9	139	72.99696	0.11276	1.86	ACS	f814w	20.9	0.01	0.39	-102.3	Cross	DClust86	
HAH J051537.3 – 432514.2	140	78.90505	-43.42074	2.87	ACS	f814w	18.1	1.88	0.70	-170.3	Arc	DClust87	0.39 P★
HAH J051856.3 – 431439.1	141	79.73450	-43.24420	4.61	ACS	f814w	20.5	0.39	0.66	72.0	Arc	DClust88	
HAH J051856.4 – 431444.4	142	79.73518	-43.24569	4.61	ACS	f814w	19.5	1.90	0.57	13.4	Arc	DClust89	

Table A.1. *continued.*

IAU Name	ID	RA	Dec	$r_{\text{arc}} (")$	instru.	filter	mag	$r_e (")$	q	PA	class	clust.	z
HAH J052116.2 – 510409.5	143	80.31740	–51.06930	0.52	ACS	f606w	23.4	0.45	0.51	–60.9	Triple	DClust90	
HAH J052214.2 – 362408.4	144	80.55929	–36.40232	1.09	ACS	f814w	21.0	0.28	0.87	23.5	Arc	DClust91	
HAH J065327.1 – 574306.1	145	103.36301	–57.71836	1.21	UVIS	f200lp	20.3	0.89	0.41	53.2	Ring	DClust92	
HAH J071718.8 + 374842.3	146	109.32870	37.81175	1.12	ACS	f814w	20.9	0.02	0.47	113.9	Arc	DClust93	
HAH J071731.9 + 374449.9	147	109.38300	37.74720	1.04	ACS	f814w	19.3	1.47	0.42	153.5	Arc	DClust94	
HAH J074704.6 + 693824.0	148	116.76942	69.64002	1.43	ACS	f606w	20.5	0.98	0.87	37.8	Arc	DClust95	
HAH J080911.4 + 064341.9	149	122.29730	6.72820	2.41	ACS	f606w	18.2	1.84	0.68	174.8	Arc	DClust96	0.36 P
HAH J083637.2 + 005332.6	150	129.15500	0.89240	3.5	ACS	f850lp	17.7	1.53	0.53	128.2	Arc		0.22 P
HAH J084349.0 + 411635.4	151	130.95433	41.27651	0.68	ACS	f814w	21.2	0.50	0.90	–110.8	Ring	DClust97	0.44 P
HAH J084959.8 + 360340.6	152	132.49950	36.06130	0.82	ACS	f814w	21.7	0.85	0.65	–16.1	Arc	DClust98	0.32 P
HAH J091023.7 + 021049.2	153	137.59885	2.18035	0.9	UVIS	f606w	22.1	0.82	0.92	–42.7	Ring	DClust99	0.69 P
HAH J091044.5 + 424945.8	154	137.68550	42.82940	1.78	ACS	f814w	20.2	0.34	0.69	15.2	Arc	DClust100	0.62 P
HAH J092141.2 – 062241.6	155	140.42165	–6.37810	0.79	ACS	f606w	22.7	0.49	0.85	–84.0	Arc	DClust101	
HAH J094058.7 + 074541.1	156	145.24482	7.76142	0.87	ACS	f814w	20.9	0.96	0.50	–40.5	Arc	DClust102	0.49 P
HAH J095557.2 – 095159.0	157	148.98830	–9.86640	1.19	ACS	f606w	21.0	0.31	0.81	67.5	Arc		
HAH J100050.2 + 013251.5	158	150.20939	1.54765	0.9	IR	f140w	19.2	0.85	0.75	152.7	Arc	DClust103	0.69 P
HAH J100142.8 + 015448.1	159	150.42840	1.91330	1.48	ACS	f814w	18.6	0.51	0.92	–65.9	Arc	DClust104	0.32 P
HAH J100222.3 + 023220.0	160	150.59303	2.53890	1.1	ACS	f814w	21.5	1.32	0.98	–164.3	Arc		1.23 P★
HAH J103943.7 – 001516.3	161	159.93217	–0.25453	1.2	ACS	f814w	20.7	1.26	0.91	–30.4	Arc		
HAH J111554.8 + 013015.5	162	168.97830	1.50430	1.09	ACS	f606w	20.6	0.56	0.68	–151.8	Arc	DClust105	0.39 P
HAH J121200.3 – 120351.1	163	170.00540	–12.06420	1.01	ACS	f606w	22.5	0.29	0.73	84.0	Arc		0.51 P
HAH J113305.2 + 500840.9	164	173.27207	50.14471	1.81	ACS	f814w	20.2	0.37	0.42	–56.3	Double	DClust106	0.4 P
HAH J114923.6 + 222926.7	165	177.34814	22.49076	2.61	ACS	f814w	16.1	4.58	0.75	50.6	Arc		0.21 S
HAH J115054.9 – 280548.7	166	177.72889	–28.09686	0.95	ACS	f814w	20.1	0.64	0.39	111.6	Arc	DClust107	
HAH J115855.4 – 185941.2	167	179.73093	–18.99480	1.55	ACS	f606w	19.3	1.22	0.29	50.2	Arc		
HAH J122027.5 + 752124.6	168	185.11459	75.35685	1.82	ACS	f850lp	19.1	0.91	0.85	77.7	Arc		
HAH J122809.5 + 221743.3	169	187.03964	22.29538	1.59	ACS	f814w	19.5	0.83	0.77	158.4	Arc		0.37 S
HAH J123227.1 – 125100.0	170	188.11304	–12.85002	1.13	ACS	f814w	20.2	0.45	0.93	–22.7	Arc		
HAH J123904.4 + 121231.4	171	189.76824	12.20872	1.73	ACS	f814w	21.4	0.39	0.81	118.2	Double		0.48 P
HAH J124355.9 + 320341.0	172	190.98280	32.06140	1.9	ACS	f814w	20.5	0.37	0.80	162.6	Arc		0.73 P
HAH J125801.0 – 431814.1	173	194.50418	–43.30393	0.85	ACS	f606w	20.4	0.50	0.57	–56.1	Arc		
HAH J130154.4 + 275347.0	174	195.47657	27.89638	1.24	ACS	f475w	22.8	0.64	0.73	43.8	Arc	DClust108	0.57 S
HAH J130236.3 + 141055.0	175	195.65149	14.18195	1.02	UVIS	f350lp	21.9	0.20	0.75	76.2	Arc	DClust109	0.51 P
HAH J133422.4 + 503133.0	176	203.59323	50.52586	1.76	ACS	f775w	20.1	0.34	0.69	9.2	Arc	DClust110	0.63 S
HAH J134711.8 – 114157.8	177	206.79914	–11.69944	2.38	ACS	f850lp	18.5	0.92	0.37	–53.0	Arc	DClust111	
HAH J135343.4 + 050952.1	178	208.43113	5.16448	1.7	ACS	f606w	20.7	0.53	0.80	159.6	Arc		0.4 P
HAH J141809.5 + 524058.8	179	214.53970	52.68300	1.89	ACS	f606w	18.9	0.99	0.76	–61.9	Arc		0.23 P
HAH J142018.4 + 530157.3	180	215.07651	53.03259	2.07	ACS	f606w	20.0	0.88	0.77	130.3	Arc		0.37 P
HAH J142952.3 + 554752.8	181	217.46790	55.79800	0.93	UVIS	f600lp	20.9	0.38	0.67	119.7	Arc	DClust112	0.6 P
HAH J143808.8 + 341940.3	182	219.53684	34.32787	3.22	ACS	f814w	19.9	0.43	0.72	75.7	Arc	DClust113	0.54 S
HAH J144727.3 + 083001.9	183	221.86388	8.50054	0.68	ACS	f606w	21.7	0.29	0.48	35.3	Arc	DClust114	0.51 P
HAH J151832.6 – 813031.8	184	229.63600	–81.50883	0.75	ACS	f814w	20.8	0.60	0.37	–59.2	Arc	DClust115	
HAH J160613.2 – 000039.5	185	241.55523	–0.01097	0.91	ACS	f606w	22.8	0.51	0.87	96.3	Ring		0.28 P
HAH J161543.8 – 060959.7	186	243.93268	–6.16660	3.09	ACS	f814w	17.5	1.57	0.92	34.9	Arc	DClust116	0.2 ★
HAH J162308.1 + 072141.5	187	245.78380	7.36153	1.74	ACS	f850lp	19.5	0.43	0.82	–55.5	Arc		0.42 P
HAH J171721.7 + 593126.0	188	259.34068	59.52392	1.67	ACS	f814w	19.1	0.89	0.95	–150.2	Arc		0.38 P
HAH J173142.8 + 225101.0	189	262.92838	22.85027	1.4	ACS	f814w	20.3	0.49	0.48	75.0	Arc	DClust117	0.36 P
HAH J173647.0 + 461847.1	190	264.19645	46.31250	2.31	IR	f110w	16.2	1.58	0.91	29.1	Arc	DClust118	
HAH J175151.7 + 443859.0	191	267.96554	44.64972	2.9	ACS	f814w	20.4	0.47	0.94	46.9	Arc	DClust119	0.38 P
HAH J221450.1 – 140049.7	192	333.70891	–14.01380	2.08	ACS	f555w	18.9	1.29	0.76	–35.5	Arc	DClust120	
HAH J224154.3 + 173336.5	193	340.47639	17.56015	0.81	ACS	f814w	19.2	0.54	0.31	87.0	Arc	DClust121	0.31 P
HAH J224901.9 – 443103.9	194	342.25819	–44.51777	1.58	ACS	f814w	21.9	0.96	0.14	–80.8	Arc	DClust122	
HAH J230104.7 + 300726.4	195	345.26983	30.12401	1.8	ACS	f850lp	17.6	1.91	0.81	26.2	Arc	DClust123	
HAH J233813.3 + 270418.0	196	354.55585	27.07173	0.58	UVIS	f814w	22.8	1.83	0.18	7.2	Double		
HAH J234232.8 – 541329.7	197	355.63659	–54.22491	1.04	ACS	f606w	22.2	0.26	0.79	–130.6	Arc	DClust124	
HAH J235747.7 + 414740.8	198	359.44843	41.79490	4.5	ACS	f814w	18.3	2.64	0.63	39.9	Arc		

Notes. This table summarises a list of characteristics related to each newly discovered lens. The lens objects are named using the standard IAU name, where the acronym HAH stands for Hubble Asteroid Hunter. They are grouped by grades (A, B, C) which were assigned by the authors of this paper as a qualitative assessment of the candidates. RA and Dec: right ascension and declination given in degrees of celestial coordinates J2000.0. r_{arc} : the arc radius (in arcsec) corresponding to the angular separation between the lens and the surrounding images. Instru. and filter: the HST instrument (ACS/WFC, WFC3/UVIS or WFC3/IR) and the filter with which the HST image was taken. Mag , r_e , q , and PA : the apparent magnitude, the effective radius (in arcsec), the axis ratio and the position angle of the foreground lens galaxy (measured from North through East, same orientation as in Figures 2-4); these parameters were retrieved with Galfit. class: the morphological class of the source images (Arc, Quad, Ring, Double). clust.: a flag indicating the presence of a foreground or background nearby cluster, details are available in table A.3. z : the photometric (P) or spectroscopic (S) redshift, retrieved from SDSS (no mark) or NED (marked ★).

Table A.2. Rediscovered lenses identified in this study.

IAU Name	ID	RA	Dec	r_{arc} (")	instru.	filter	mag	r_e (")	q	PA	class	clust.	z	reference
A grade Lenses														
HAH J001426.3 – 302255.3	199	3.60962	–30.38202	1	ACS	f814w	18.9	0.55	0.72	–137.7	Arc	RClust125	0.24 ★	Pawase et al. (2014)
HAH J015242.4 – 135618.2	200	28.17683	–13.93838	0.97	ACS	f775w	21.4	0.30	0.92	–96.3	Arc	RClust126		Grillo et al. (2008)
HAH J032940.8 – 021318.5	201	52.42010	–2.22180	0.82	ACS	f435w	22.2	0.67	0.94	–148.2	Arc	RClust127		Desprez et al. (2018)
HAH J033238.2 – 275653.3	202	53.15930	–27.94810	1.67	ACS	f606w	21.0	1.08	0.53	–124.5	Arc			More et al. (2011)
HAH J033304.4 – 065144.3	203	53.26850	–6.86230	0.83	IR	f160w	19.7	0.69	0.75	104.2	Arc	RClust128	0.57 P	Sharon et al. (2020)
HAH J041604.1 – 240522.2	204	64.01720	–24.08950	1.2	ACS	f814w	20.0	0.57	0.32	28.6	Arc	RClust129	0.4 P★	Diego et al. (2015)
HAH J045400.6 – 030833.8	205	73.50260	–3.14280	1.88	ACS	f814w	17.0	3.45	0.69	–8.6	Arc	RClust130		Schirmer et al. (2010)
HAH J045413.1 + 025733.8	206	73.55475	2.95939	2.6	ACS	f814w	16.5	2.55	0.96	–3.0	Ring	RClust131		Clowe et al. (2012)
HAH J074450.9 + 392736.0	207	116.21211	39.45986	unfit	ACS	f606w	22.5	1.43	0.39	21.7	Arc	RClust132	0.62 P★	Horesh et al. (2010)
HAH J091617.5 – 002405.9	208	139.07306	–0.40164	0.74	ACS	f814w					Arc	RClust133		Clowe et al. (2012)
HAH J095921.8 + 020638.5	209	149.84068	2.11064	0.71	ACS	f814w	20.5	0.34	0.78	49.4	Quad		0.58 P	Faure et al. (2008)
HAH J095930.9 + 023427.8	210	149.87890	2.57440	0.92	ACS	f814w	21.9	0.38	0.61	–69.8	Arc		0.89 ★	Lagattuta et al. (2010)
HAH J095956.0 + 021901.8	211	149.98330	2.31719	2.36	ACS	f814w	22.9	4.65	0.21	10.7	Arc		0.93 ★	More et al. (2012)
				2.36	ACS	f814w	21.3	0.74	0.88	–64.5	Arc		0.93 ★	
HAH J100012.6 + 022015.8	212	150.05258	2.33772	0.73	ACS	f814w	19.3	0.49	0.81	5.9	Arc	RClust134	0.37 P	Cabanac et al. (2007)
HAH J100018.5 + 023845.6	213	150.07700	2.64600	1.51	ACS	f814w	23.6	0.12	0.71	10.8	Arc	RClust135	0.42 P★	Cabanac et al. (2007)
HAH J100108.4 + 024029.9	214	150.28495	2.67496	1.41	ACS	f814w	19.3	0.34	0.86	1.8	Arc		0.32 P★	Pourrahmani et al. (2018)
HAH J100133.7 + 022135.3	215	150.39058	2.35982	2.54	ACS	f814w	20.3	0.54	0.44	–29.4	Arc	RClust136	0.36 P	More et al. (2012)
HAH J100211.2 + 021139.5	216	150.54675	2.19429	3.45	ACS	f814w	20.5	1.77	0.46	13.7	Arc		0.7 P	Faure et al. (2008)
HAH J114936.7 + 222612.0	217	177.40280	22.43667	0.859	ACS	f814w	19.8	0.48	0.80	60.8	Cross		0.5 P	Desprez et al. (2018)
HAH J133235.0 + 503237.3	218	203.14564	50.54369	4.2	ACS	f606w	18.9	1.66	0.72	–156.6	Arc		0.28 S	Ragozzine et al. (2012)
HAH J133241.0 + 503346.3	219	203.17064	50.56286	2.52	ACS	f606w	18.2	1.89	0.90	149.3	Ring	RClust137	0.28 S	Ragozzine et al. (2012)
HAH J135409.1 + 771557.2	220	208.53795	77.26590	1.79	ACS	f814w	21.0	0.60	0.75	–179.5	Arc	RClust138		Repp & Ebeling (2018)
HAH J135409.2 + 771549.9	221	208.53816	77.26385	2.26	ACS	f814w	20.5	0.91	0.65	–90.1	Arc	RClust139		Repp & Ebeling (2018)
HAH J140237.0 + 542716.3	222	210.65450	54.45455	1.8	ACS	f814w	18.1	1.14	0.74	–114.1	Arc			Pawase et al. (2014)
HAH J141735.7 + 522646.3	223	214.39891	52.44621	1.6	ACS	f814w	20.2	0.98	0.62	–142.5	Cross		0.59 P	Ratnatunga et al. (1995)
HAH J141820.8 + 523611.1	224	214.58664	52.60309	0.81	ACS	f814w	21.2	0.62	0.76	–91.0	Arc		0.58 S	Moustakas et al. (2007)
HAH J143703.3 + 350153.3	225	219.26352	35.03145	0.65	ACS	f814w	22.5	0.36	0.76	–78.8	Ring		0.56 P	Pawase et al. (2014)
HAH J145250.0 + 580135.3	226	223.20849	58.02649	3.22	ACS	f814w	18.3	1.17	0.67	42.3	Arc	RClust140	0.32 S	Repp & Ebeling (2018)
HAH J152745.2 + 065220.8	227	231.93830	6.87247	1.78	UVIS	f606w	22.0	0.30	0.33	39.7	Arc	RClust141	0.32 P	Koester et al. (2010)
HAH J213512.7 – 010143.9	228	323.80296	–1.02886	0.98	ACS	f814w	20.7	0.64	0.65	98.8	Arc	RClust142	0.3 P	Smail et al. (2007)
HAH J221142.0 – 035052.4	229	332.92486	–3.84790	1.15	ACS	f814w	21.7	0.19	0.77	–67.4	Cross	RClust143	0.42 P	Bettoni et al. (2019)
HAH J224851.7 – 443105.1	230	342.21568	–44.51858	3.17	ACS	f814w	20.9	0.11	0.82	33.3	Arc	RClust144	0.33 ★	Guzzo et al. (2009)
				3.17	ACS	f814w	17.7	2.40	0.82	–103.8	Arc		0.33 ★	
				3.17	ACS	f814w	19.0	3.39	0.86	–10.8	Arc		0.33 ★	
				3.17	ACS	f814w	20.1	0.27	0.69	–32.1	Arc		0.33 ★	
HAH J235130.6 – 261500.7	231	357.87744	–26.25008	3.32	ACS	f814w	16.3	4.47	0.74	–124.2	Arc		0.27 ★	Pawase et al. (2014)
B grade Lenses														
HAH J001423.0 – 302109.7	232	3.59578	–30.35270	1.7	ACS	f814w	19.8	0.83	0.85	22.5	Arc	RClust145	0.25 ★	Pawase et al. (2014)
HAH J033153.2 – 274619.3	233	52.97181	–27.77194	1.05	ACS	f840w	20.7	0.66	0.76	–62.5	Arc		0.73 ★	More et al. (2011)
HAH J095939.1 + 023044.1	234	149.91311	2.51224	1.7	ACS	f814w	20.0	0.76	0.69	62.6	Arc	RClust146	0.72 P	Faure et al. (2008)
HAH J100013.9 + 022249.8	235	150.05800	2.38050	1.65	ACS	f606w	19.3	1.90	0.79	–110.8	Arc	RClust147	0.35 S	Faure et al. (2008)
HAH J100047.7 + 015023.3	236	150.19854	1.83981	1.71	ACS	f814w	20.6	0.75	0.72	2.2	Arc	RClust148	0.89 ★	Faure et al. (2008)
HAH J100055.7 + 013821.1	237	150.23214	1.63919	1.06	ACS	f814w	20.9	0.35	0.95	92.4	Arc	RClust149	0.55 P	Faure et al. (2008)
HAH J100056.8 + 021225.8	238	150.23661	2.20719	1.67	ACS	f814w	18.8	1.01	0.66	64.1	Arc		0.36 S	Faure et al. (2008)
HAH J103751.4 – 124326.3	239	159.46400	–12.72398	1.12	ACS	f814w	19.5	1.39	0.70	–49.2	Arc		0.58 ★	Pawase et al. (2014)
				1.12	ACS	f814w	19.8	0.66	0.86	–53.7	Arc		0.58 ★	
HAH J121228.4 – 121723.1	240	183.11829	–12.29002	2.84	ACS	f814w	21.9	0.18	0.79	–105.5	Arc			Ebeling et al. (2019)
				2.84	ACS	f814w	20.1	1.03	0.84	–175.4	Arc			
HAH J123729.9 + 621300.7	241	189.37456	62.21685	2.12	ACS	f814w	19.9	0.81	0.91	48.9	Arc		0.49 P	Fassnacht et al. (2004)
HAH J130042.7 + 280523.6	242	195.17804	28.08989	1.08	ACS	f814w	18.2	1.70	0.61	–118.2	Arc	RClust150	0.37 S	Pawase et al. (2014)
HAH J131829.4 – 010421.6	243	199.62246	–1.07267	0.67	ACS	f814w	19.9	0.67	0.84	–85.0	Arc		0.66 S	Brownstein et al. (2012)
HAH J141833.1 + 524352.5	244	214.63790	52.73126	0.69	ACS	f814w	20.5	1.32	0.68	97.2	Arc		0.47 P	Marshall et al. (2009)
HAH J214014.8 – 233904.3	245	325.06171	–23.65125	2.58	ACS	f606w	20.0	0.58	0.94	133.2	Arc			Fort et al. (1992)
HAH J230824.7 – 021213.3	246	347.10300	–2.20370	3.24	ACS	f606w	18.2	2.76	0.53	–88.3	Arc	RClust151	0.27 P	Jacobs et al. (2019)
C grade Lenses														
HAH J013152.3 – 133658.3	247	22.96793	–13.61621	1.9	ACS	f475w	19.0	1.58	0.86	–170.7	Arc	RClust152		Zitrin et al. (2015)
HAH J071815.0 + 374200.3	248	109.56253	37.70009	1.91	ACS	f814w	20.6	0.44	0.96	61.4	Arc	RClust153	0.34 P	Ebeling et al. (2014)
HAH J095810.1 + 022942.0	249	149.54211	2.49500	2.21	ACS	f814w	18.9	1.05	0.75	–57.8	Arc		0.4 P	Jackson (2008)
HAH J114934.3 + 222440.5	250	177.39310	22.41127	0.61	ACS	f606w	23.1	0.67	0.93	7.0	Arc	RClust154	0.47 P	Morishita et al. (2017)
HAH J173217.5 + 193250.3	251	263.07333	19.54731	1.2	ACS	f814w	19.8	0.61	0.93	44.6	Arc	RClust155		Ebeling et al. (2018)
HAH J203146.3 – 403705.4	252	307.94293	–40.61818	1.02	ACS	f814w	22.4	0.30	0.76	0.2	Arc	RClust156		Richard et al. (2015)

Notes. This table summarises a list of characteristics related to each rediscovered lens. The lens objects are named using the standard IAU name, where the acronym HAH stands for Hubble Asteroid Hunter. The lenses are grouped by grades (A,B,C) which were assigned by the authors of this paper as a qualitative assessment of the candidates. RA and Dec: right ascension and declination given in degrees of celestial coordinates J2000.0. r_{arc} : the arc radius (in arcsec) corresponding to the angular separation between the lens and the surrounding images. Instru. and filter: the HST instrument (ACS/WFC, WFC3/UVIS or WFC3/IR) and the filter with which the HST image was taken. Mag, r_e , q , and PA: the apparent magnitude, the effective radius (in arcsec), the axis ratio and the position angle of the foreground lens galaxy (measured from North through East, same orientation as in Figures 2–4); these parameters were retrieved with GalFit. class: the morphological class of the source images (Arc, Quad, Ring, Double). clust.: a flag indicating the presence of a foreground or background nearby cluster, details are available in table A.3. z : the photometric (P) or spectroscopic (S) redshift, retrieved from SDSS (no mark) or NED (marked ★). The reference columns shows the paper where the the strong lensing system is mentioned, as listed by the ESASky portal. Because of the complexity of lens ID 207, we did not manage to measure its arc radius. Finally, We did not manage to obtain a good model for the lens ID 208 and, therefore, left the GALFIT parameters blank.

Table A.3. Candidate cluster flags.

Flag	IAU name	HST Observation Target	DESI Catalog		redMaPPer SDSS Catalog	
		Targeted Cluster ID	Candidate Cluster ID	Distance (")	Candidate Cluster ID	Distance (")
Discovery group						
DClust1	HAH J002348.6 – 244149.6		3469200139	84		
DClust2	HAH J002753.2 – 753730.0	SMACS J0028.2 – 7537				
DClust3	HAH J004924.3 – 205729.8	ESO 540 – 31	3316000106	93		
DClust4	HAH J015949.3 – 084906.0	MACS J0159.8 – 0849	2830900043	64	RM J015949.3 – 084958.9	53
DClust5	HAH J024329.8 – 593102.7	SPT-CL J0243 – 5930				
DClust6	HAH J024533.6 – 530203.5	ACO S295	4427400112	36		
DClust7	HAH J025241.6 – 150025.5		3087900009	30		
DClust8	HAH J025659.9 – 163059.5		3164700123	32		
DClust9	HAH J034445.2 – 642133.8	SPT-CL J0345 – 6419				
DClust10	HAH J054707.0 – 390516.3	MACS J0547.0 – 3904	3986900096	67		
DClust11	HAH J061345.7 – 562750.4	SPT-CL J0613 – 5627	4505800076	0		
DClust12	HAH J072221.9 + 072326.7	PSZ2 G209.79 + 10.23				
DClust13	HAH J083420.3 + 452506.9		692800146	70	RM J083416.3 + 452420.0	63
DClust14	HAH J102914.8 + 262207.0		1355200029	92		
DClust15	HAH J105722.7 + 580046.5		369000033	92		
DClust16	HAH J111337.4 + 221249.2	A1300				
DClust17	HAH J114938.4 + 222107.7		1510200105	161	RM J114935.7 + 222354.6	172
DClust18	HAH J131953.6 + 700420.8	MACS J1319.9 + 7003	157400151	75		
DClust19	HAH J133525.9 + 405952.4	ACO 1763	846500034	14	RM J133520.1 + 410004.1	67
DClust20	HAH J141139.2 + 565200.9		4066000086	80		
DClust21	HAH J214817.6 – 484350.5	SPT-CL J2148 – 4843				
DClust22	HAH J234106.5 – 000007.5		2470000044	141		
DClust23	HAH J001419.9 – 302600.7	Abell 2744				
DClust24	HAH J002706.3 + 170313.5		1728400102	48		
DClust25	HAH J003350.8 – 074959.9	MACS J0033.8 – 0751	2778200022	75	RM J003353.1 – 075210.4	135
DClust26	HAH J004426.2 – 403941.4	SPT-CL J0044 – 4037	4058400124	140		
DClust27	HAH J005141.6 + 272001.5	MACS J0051.6 + 2720	1319300120	49	RM J005138.6 + 271959.9	40
DClust28	HAH J011138.3 – 454015.1		4208300009	70		
DClust29	HAH J013723.7 – 082852.2	WHL J013719.8 – 082841	2804900125	78	RM J013725.0 – 082722.7	92
DClust30	HAH J023951.1 – 013205.9		2498800056	177	RM J023952.7 – 013418.9	135
DClust31	HAH J024535.7 – 530125.5	ACO S295	4427400112	36		
DClust32	HAH J025735.5 – 220928.5		3369500071	55		
DClust33	HAH J025740.9 – 221027.3		3369500071	55		
DClust34	HAH J032030.9 + 003242.8		2422800030	88		
DClust35	HAH J033530.7 – 540734.7		4447600038	41		
DClust36	HAH J033645.9 – 535536.7		4428100085	63		
DClust37	HAH J035851.7 – 295418.7	MACS J0358.8 – 2955	3677800030	79		
DClust38	HAH J041631.5 – 240512.5	MACS J0416.1 – 2403				
DClust39	HAH J044208.3 – 281503.7	RCS J044207 – 2815.0	3601800082	150		
DClust40	HAH J045430.7 – 030133.2		2578000137	128		
DClust41	HAH J045441.7 – 030319.9		2578000137	142		
DClust42	HAH J051850.3 – 431442.0		4114300083	60		
DClust43	HAH J055326.6 – 334254.0	MACS J0553.4 – 3342	3807900148	98		
DClust44	HAH J072218.2 + 072314.8	PSZ2 G209.79 + 10.23				
DClust45	HAH J072333.8 – 732550.9	SMACS J0723.3 – 7327				
DClust46	HAH J084712.7 + 344910.9		1046200011	65		
DClust47	HAH J094949.9 + 170614.4	RXC J0949.8 + 1707	1738400144	51	RM J094951.8 + 170710.6	62
DClust48	HAH J095803.9 + 653409.1		2166000094	17		
DClust49	HAH J100030.1 + 023716.7		2353000132	98		
DClust50	HAH J100124.2 + 555407.2		421600140	67		
DClust51	HAH J104132.0 + 000125.0		2456200026	114		
DClust52	HAH J105726.9 + 575944.0		369000033	92		
DClust53	HAH J111507.3 + 531955.8	MACS J1115.2 + 5320	499300020	79	RM J111514.8 + 531954.6	67
DClust54	HAH J111822.1 + 033802.1				RM J111814.9 + 033931.6	141
DClust55	HAH J122944.7 + 112238.3		1971700080	99		
DClust56	HAH J123618.8 + 260905.0		1383000036	68		
DClust57	HAH J125907.8 – 014439.0	Abell 1650 – 9 – 13 – 0				
DClust58	HAH J130152.7 + 275147.7		1306700027	151		
DClust59	HAH J132217.5 + 464630.4		674100042	62	RM J132226.8 + 464630.2	95
DClust60	HAH J132331.9 + 302155.8		1204700022	63	RM J132334.1 + 302249.2	60
DClust61	HAH J133240.6 + 503315.5	Abell 1758N – P2	563100075	67	RM J133238.4 + 503336.0	29
DClust62	HAH J133252.7 + 503026.9	Abell 1758N – P1	563100075	142		
DClust63	HAH J135953.3 + 623118.4		275000026	34	RM J135950.6 + 623105.5	23
DClust64	HAH J143236.3 + 344030.4		1052300092	59		
DClust65	HAH J145832.7 – 002349.9		2486400029	55		
DClust66	HAH J151841.7 + 084549.2		2102700082	55	RM J151846.8 + 084550.5	75
DClust67	HAH J161311.2 + 565004.1		408100043	44		
DClust68	HAH J162122.2 + 381006.5	MACS J1621.3 + 3810	926200081	35	RM J162124.8 + 381008.9	30
DClust69	HAH J173146.2 + 225237.6		1516300115	87		
DClust70	HAH J180652.4 + 292945.3		1260900074	29		
DClust71	HAH J191700.9 – 333207.0	PLCK ESZ G004.5 – 19.5 ACS				
DClust72	HAH J191709.5 – 333127.0	PLCK ESZ G004.5 – 19.5 IR				
DClust73	HAH J224324.6 – 093617.3	MACS J0717 + 3745 ACS	2878600004	43	RM J224319.8 – 093530.9	85
DClust74	HAH J233220.8 – 535909.8	SMACS J2332.4 – 5358	4463600107	84		
DClust75	HAH J000146.0 – 544026.2	SPT-CL J0001 – 5440	4444800055	89		
DClust76	HAH J002357.7 – 244154.3		3469200139	84		
DClust77	HAH J003501.7 + 023358.6	MACS J0034.9 + 0234	2343000008	64	RM J003457.8 + 023331.8	64
DClust78	HAH J013726.6 – 082747.9	WHL J013719.8 – 082841	2804900125	78	RM J013725.0 – 082722.7	35
DClust79	HAH J015246.7 + 360750.5	NGC 708				
DClust80	HAH J015317.2 – 135220.6		3035600139	99		

Table A.3. *continued.*

Flag	IAU name	HST Observation Target	DESI Catalog		redMaPPer SDSS Catalog	
		Targeted Cluster ID	Candidate Cluster ID	Distance (")	Candidate Cluster ID	Distance (")
DClust81	HAH J023726.4 – 262957.6	RXC J0237.4 – 2630	3548400119	30		
DClust82	HAH J024336.7 – 483319.4	SPT-CL J0243 – 4833	4279300045	50		
DClust83	HAH J030901.7 + 264522.2	MACS J0308.9 + 2645				
DClust84	HAH J042905.4 – 101206.7		2884800097	71		
DClust85	HAH J043916.2 – 460115.2	SMACS J0439.2 – 4600	4211700086	25		
DClust86	HAH J045159.3 + 000645.9	MACS J0451.9 + 0006	2449900135	66		
DClust87	HAH J051537.3 – 432514.2		4139400014	36		
DClust88	HAH J051856.3 – 431439.1		4114300083	60		
DClust89	HAH J051856.4 – 431444.4		4114300083	60		
DClust90	HAH J052116.2 – 510409.5	SPT-CL J0521 – 5104	4368600053	42		
DClust91	HAH J052214.2 – 362408.4		3909700155	34		
DClust92	HAH J065327.1 – 574306.1	SPT-CL J0653 – 5744				
DClust93	HAH J071718.8 + 374842.3	MACS J071718 + 374841				
DClust94	HAH J071731.9 + 374449.9		942200072	56		
DClust95	HAH J074704.6 + 693824.0		154800014	33		
DClust96	HAH J080911.4 + 064341.9		2171900062	158		
DClust97	HAH J084349.0 + 411635.4		841300099	63		
DClust98	HAH J084959.8 + 360340.6		995000060	103	RM J085007.9 + 360413.7	103
DClust99	HAH J091023.7 + 021049.2		2377800058	84		
DClust100	HAH J091044.5 + 424945.8		790800062	36		
DClust101	HAH J092141.2 – 062241.6		2736400046	119		
DClust102	HAH J094058.7 + 074541.1	MACS J0940 ACS	2122300012	118	RM J094053.7 + 074425.4	107
DClust103	HAH J100050.2 + 013251.5		2378700125	131		
DClust104	HAH J100142.8 + 015448.1		2378700108	99		
DClust105	HAH J111554.8 + 013015.5	MACS J1115.8 + 0129	2380000092	49		
DClust106	HAH J113305.2 + 500840.9	MACS J1133.2 + 5008	561400014	31	RM J113313.2 + 500840.5	76
DClust107	HAH J115054.9 – 280548.7	PLCK ESZ G287.0 + 32.9				
DClust108	HAH J130154.4 + 275347.0		1306700027	105		
DClust109	HAH J130236.3 + 141055.0		1869900048	112		
DClust110	HAH J133422.4 + 503133.0	RX J1334.5 + 5030 POS1	563100033	34		
DClust111	HAH J134711.8 – 114157.8	RX J1347 – 1145 ACS				
DClust112	HAH J142952.3 + 554752.8		425100125	106		
DClust113	HAH J143808.8 + 341940.3		1078000014	143		
DClust114	HAH J144727.3 + 083001.9	MACS J1447.4 + 0827	2102100021	88	RM J144726.0 + 082825.1	99
DClust115	HAH J151832.6 – 813031.8	PLCK ESZ G308.3 – 20.2				
DClust116	HAH J161543.8 – 060959.7	Abell 2163				
DClust117	HAH J173142.8 + 225101.0	MACS J1731.6 + 2252	1516300115	87		
DClust118	HAH J173647.0 + 461847.1		678200065	0		
DClust119	HAH J175151.7 + 443859.0	MACS J1752.0 + 4440	750100068	78		
DClust120	HAH J221450.1 – 140049.7	MACS J2214 – 1359	3057300114	117		
DClust121	HAH J224154.3 + 173336.5	MACS J2241.8 + 1732	1726600046	86	RM J224158.1 + 173303.7	63
DClust122	HAH J224901.9 – 443103.9		4206000045	167		
DClust123	HAH J230104.7 + 300726.4		1240500156	73		
DClust124	HAH J234232.8 – 541329.7	SPT-CL J2342 – 5411				
Rediscovery group						
RClust125	HAH J001426.3 – 302255.3		3673800147	109		
RClust126	HAH J015242.4 – 135618.2		3035600098	64		
RClust127	HAH J032940.8 – 021318.5		2550900117	118		
RClust128	HAH J033304.4 – 065144.3		2730200015	38		
RClust129	HAH J041604.1 – 240522.2		3473300094	120		
RClust130	HAH J045400.6 – 030833.8		2578000063	118		
RClust131	HAH J045413.1 + 025733.8	Abell 520 P1				
RClust132	HAH J074450.9 + 392736.0		891500113	54		
RClust133	HAH J091617.5 – 002405.9	MACS J0916.1 – 0023	2480300042	110	RM J091617.6 – 002405.7	0
RClust134	HAH J100012.6 + 022015.8		2353000151	104		
RClust135	HAH J100018.5 + 023845.6		2353000132	98		
RClust136	HAH J100133.7 + 022135.3		2353000126	140		
RClust137	HAH J133241.0 + 503346.3		563100075	87	RM J133238.4 + 503336.0	26
RClust138	HAH J135409.1 + 771557.2	MACS J1354.6 + 7715				
RClust139	HAH J135409.2 + 771549.9	MACS J1354.6 + 7715	58300091	50		
RClust140	HAH J145250.0 + 580135.3	MACS J1452.9 + 5802	371800109	112		
RClust141	HAH J152745.2 + 065220.8		2179700063	16	RM J152745.8 + 065233.6	16
RClust142	HAH J213512.7 – 010143.9		2519000027	169	RM J213512.2 – 010255.8	72
RClust143	HAH J221142.0 – 035052.4		2622000023	115	RM J221145.9 – 034944.5	90
RClust144	HAH J224851.7 – 443105.1		4206000045	58		
RClust145	HAH J001423.0 – 302109.7		3673800147	109		
RClust146	HAH J095939.1 + 023044.1		2353000051	48		
RClust147	HAH J100013.9 + 022249.8		2353000156	124		
RClust148	HAH J100047.7 + 015023.3		2378700136	94		
RClust149	HAH J100055.7 + 013821.1		2378700129	169		
RClust150	HAH J130042.7 + 280523.6		1306700012	111		
RClust151	HAH J230824.7 – 021213.3		2571800113	28	RM J230822.2 – 021131.8	56
RClust152	HAH J013152.3 – 133658.3		3009600047	58		
RClust153	HAH J071815.0 + 374200.3		942200005	24		
RClust154	HAH J114934.3 + 222440.5		1510200105	63	RM J114935.7 + 222354.6	50
RClust155	HAH J173217.5 + 193250.3		1644300126	114		
RClust156	HAH J203146.3 – 403705.4		4079500042	96		

Notes. Candidate clusters from Tables A.1 and A.2. As the presence of nearby clusters could provoke excess lensing substructures, we report the confirmed and targeted clusters from the HST observations, as well as candidate clusters identified by cross-matching within a 3' radius with DESI (Zou et al. 2021) and redMaPPer on SDSS (Rykoff et al. 2014, 2016) catalogues.

Appendix B: GALFIT modelling of light profiles of lenses

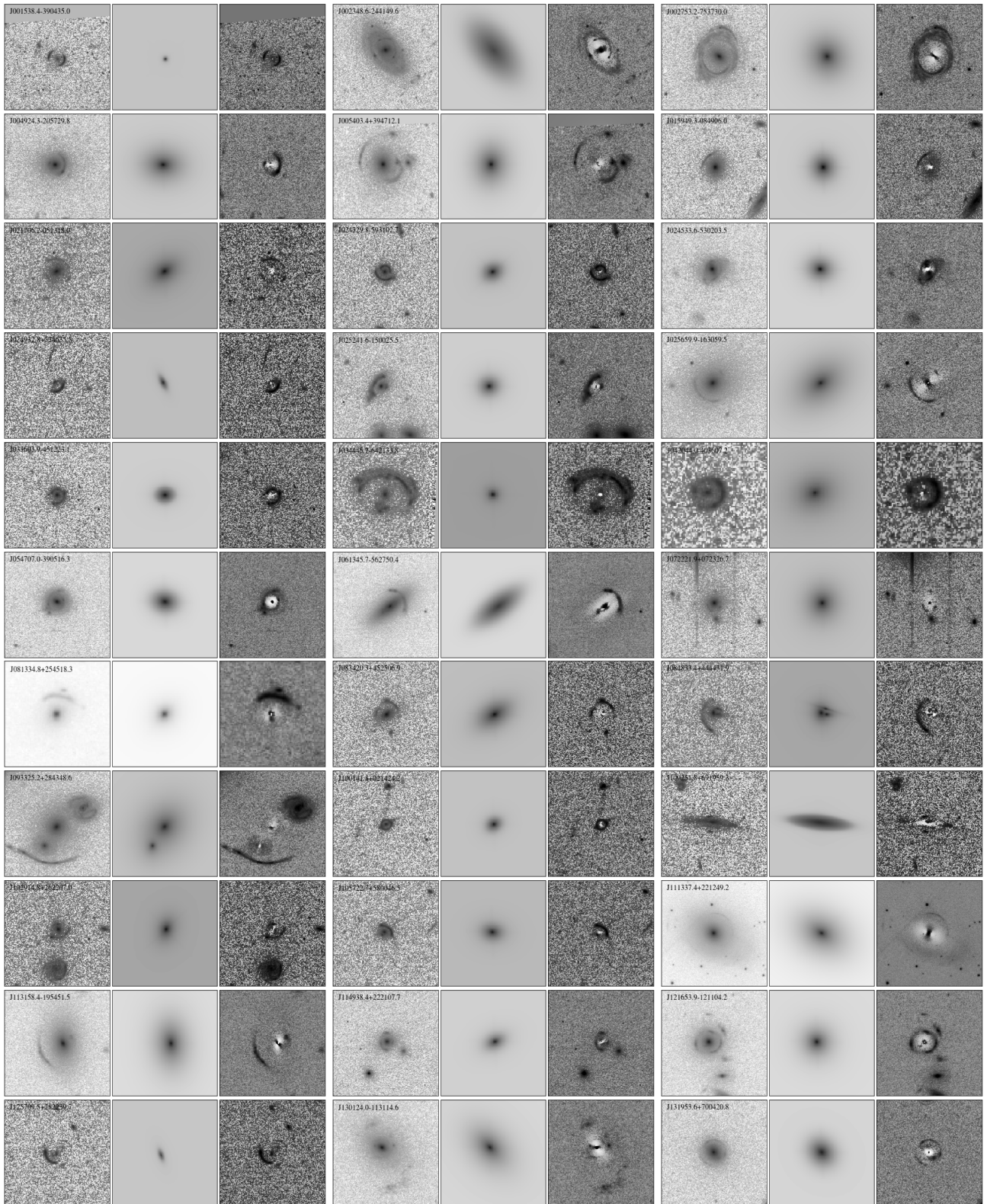


Fig. B.1. Postage stamps showing the lens galaxy fitting with GALFIT for the newly-discovered HAH grade A candidates. We present three lens candidates per line, where each HAH lens is indicated by the sequence part of the name. Each postage stamp is composed by (1) the original image used for the fit, using the HST instruments and filters indicated in Tables A.1 and A.2, (2) the fitted model using chi-square minimisation in GALFIT, (3) the residuals obtained by subtracting the fitted model from the original image. The arcs and background galaxies were masked using SExtractor during the fitting process, such that only the light of the lens was fitted. The postage stamps show the default orientation of the HST images, which can be different from the one shown in Figure 2.

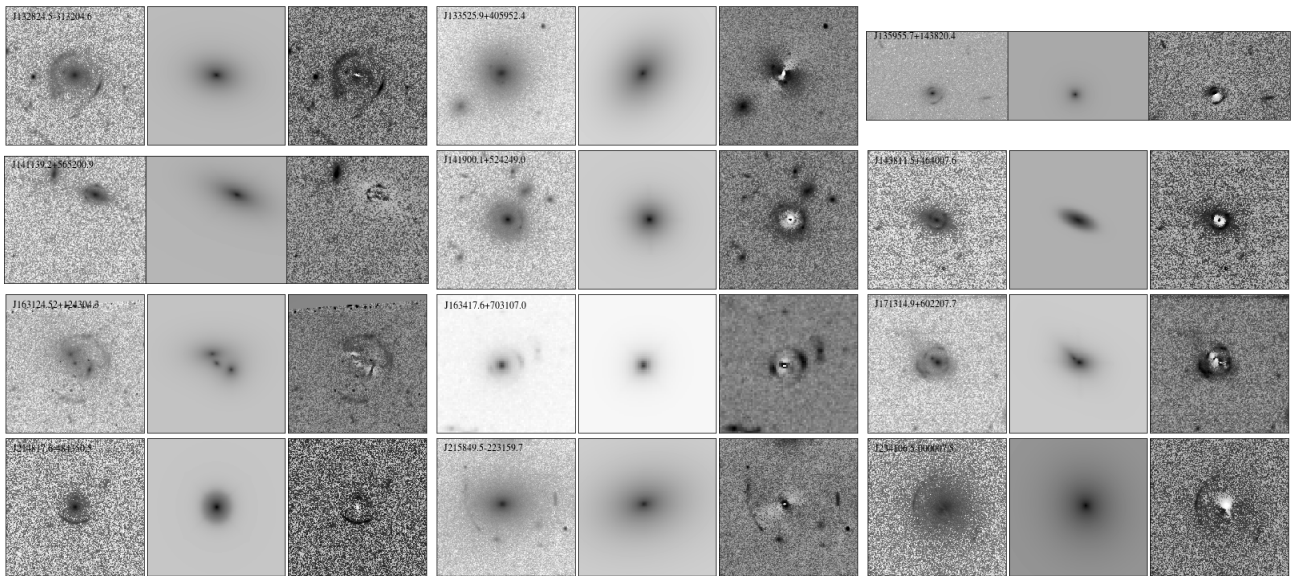


Fig. B.2. *continued.*

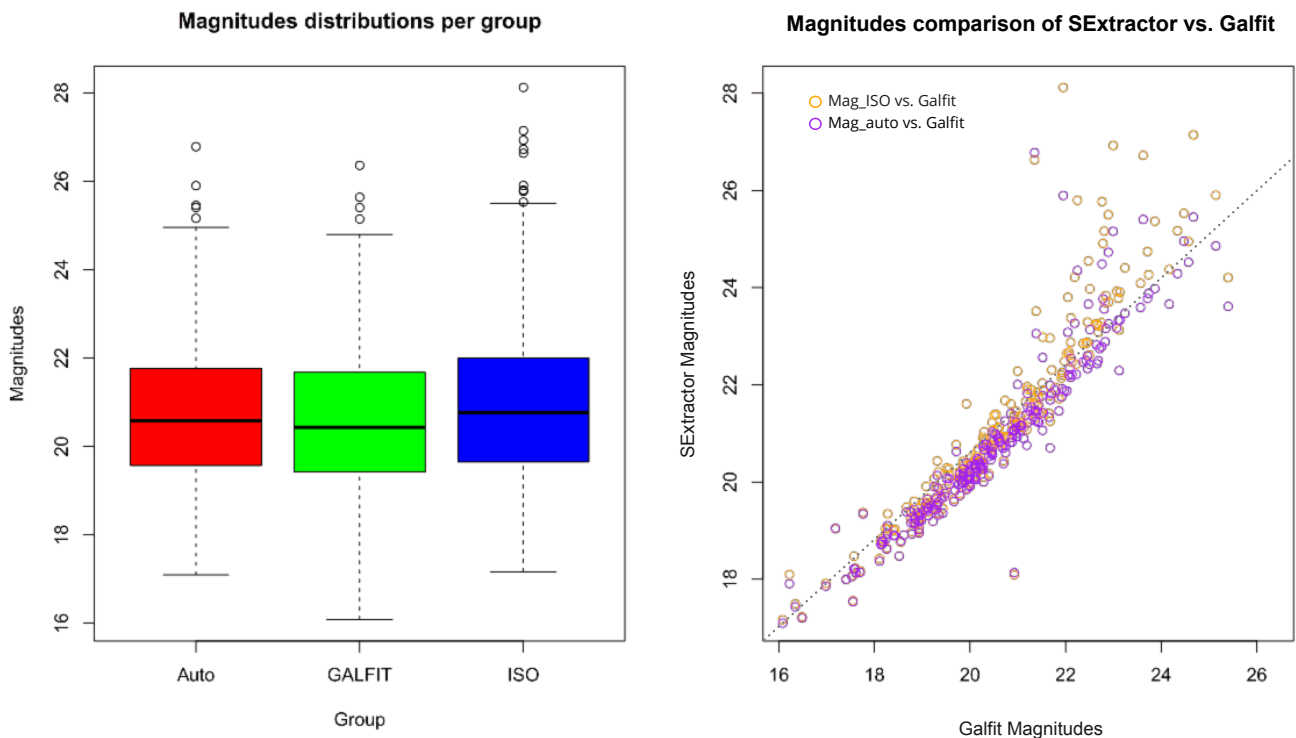


Fig. B.3. *Left:* Boxplots representing the distributions of the magnitudes measured with `Galfit` and the `Auto` and `ISO` magnitudes measured with `SExtractor`. For each boxplot, the middle line in the box represent the median of the distribution. The box itself extends from the lower quartile to the upper quartile, covering the interquartile range. The points which fall outside the whiskers situated on each side of the box are considered to be extreme values. *Right:* Comparison between the magnitudes measured with `Galfit` (abscissa) against the `'ISO'` and `'Auto'` magnitudes (ordinates) from `SExtractor`. The grey dotted line is a 45° guide line. These two plots do not show systematic differences in the photometry of the foreground lens galaxies between the different measurements.

Appendix C: Additional lens candidates

After the end of the Hubble Asteroid Hunter citizen science project, we found twelve serendipitous non-targeted lens candidates from recent imaging observations released in the HST archives after June 2020 (Table C.1 and Fig. C.1). These candidates were identified by citizen scientist Claude Cornen, by inspecting the 'Daily Data Reports'⁹, while discarding calibrations as well as observations of asteroids, comets, stars or clusters.

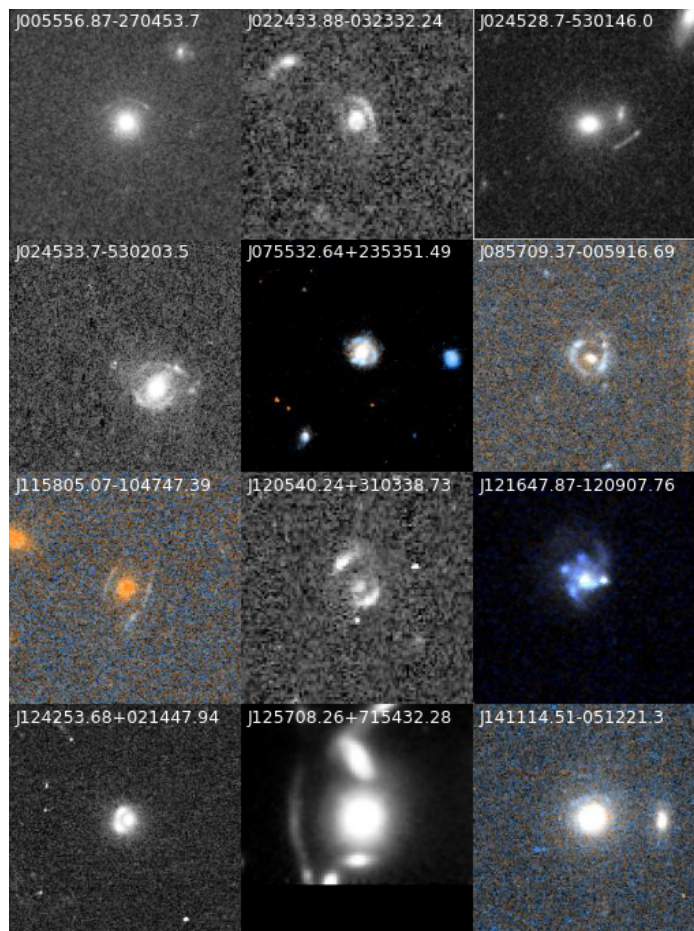


Fig. C.1. Serendipitous, non-targeted lens candidates identified after the end of the Hubble Asteroid Hunter citizen science project, not included in the main analysis of the paper. The HAH lenses from the mosaics are indicated using only the sequence part of their name.

Table C.1. New strong lens candidates identified after the end of the Hubble Asteroid Hunter citizen science project.

Candidate (IAU name)	Obs. id	Obs. date	Instrument	Apertures	Filters	Proposal id	Grade
HAH J005556.9-270453.7	ie6jy6010	2020-06-01	WFC3	IR	F140W	15347	B
HAH J022433.88-032332.24	jeco01010	2021-09-15	ACS	WFC	F475W	16300	C
HAH J024528.7-530146.0	iepl29020	2022-02-04	WFC3	UVIS	F606W	16729	C
HAH J024533.7-530203.5	iepl29020	2022-02-04	WFC3	UVIS	F606W	16729	A
HAH J075532.64+235351.49	jece46020	2021-03-12	ACS	WFC	F814W	16257	B
HAH J085709.37-005916.69	jea302010	2021-04-07	ACS	WFC	F814W	16186	A
HAH J115805.07-104747.39	jeh903010	2021-04-08	ACS	WFC	F814W	16429	A
HAH J120540.24+310338.7	jdrz1h010	2021-05-26	ACS	WFC	F606W	15446	A
HAH J121647.87-120907.76	jc8h07020	2014-06-05	ACS	WFC	F814W	13393	C
HAH J124253.68+021447.94	jece02010	2021-04-12	ACS	WFC	F606W	16257	B
HAH J125708.26+715432.28	ieer07010	2021-01-02	WFC3	IR	F110W	16243	B
HAH J141114.51-051221.3	jece78020	2021-04-18	ACS	WFC	F814W	16257	C

Notes. IAU names, observing programs, HST instruments and filters corresponding to new strong lens candidates identified after the end of the Hubble Asteroid Hunter citizen science project, from data released in the HST archives after June 2020.

⁹ <https://archive.stsci.edu/hst/daily/>